Data-Driven Molecular Dynamics and TEM Analysis of Platinum Crystal Growth on Graphene and Reactive Hydrogen-Sensing Dynamics

Akram Ibrahim,[1] Ahmed M. Hafez,[2,3] Mahmooda Sultana,[4] and Can Ataca[1]

[1])*Department of Physics, University of Maryland Baltimore County, Baltimore, Maryland 21250, United States*

[2])*Center for Research and Exploration in Space Science and Technology, NASA Goddard Space Flight Center, Greenbelt, Maryland 20771, United States*

[3])*Department of Astronomy, University of Maryland College Park, College Park, Maryland 20742, United States*

[4])*Planetary Environments Laboratory, NASA Goddard Space Flight Center, Greenbelt, Maryland 20771, United States*

(Dated: 9 April 2025)

Platinum-functionalized graphene harnesses graphene's exceptional carrier mobility alongside platinum's catalytic activity for hydrogen sensing; however, the mechanisms governing Pt crystal growth, its interaction with graphene, and the consequent impact on hydrogen sensitivity remain incompletely understood. Here, we develop a high-fidelity equivariant machine-learned interatomic potential (MLIP) to perform large-scale molecular dynamics (MD) simulations with near–density functional theory (DFT) accuracy. Our simulations capture key growth stages—including Pt nucleation, coalescence, and the formation of either polycrystalline clusters or epitaxial thin films—under varying deposition loadings and rates. Transmission electron microscopy and Raman measurements validate the predicted morphologies, showing that at lower Pt loadings the structures consist predominantly of small approximately spherical clusters, which transition to slightly thicker, more planar domains as Pt loading increases. Reactive MD simulations show that hydrogen primarily dissociates on Pt nanostructures with negligible spillover onto pristine graphene at room temperature. Moreover, we identify correlations between Pt coverage and hydrogen adsorption kinetics: hydrogen uptake increases with Pt loading at a diminishing rate, while reaction kinetics are significantly faster at lower coverages and decline rapidly with increasing loading. Our DFT simulations reveal that undercoordinated Pt clusters induce n-type doping in graphene. However, hydrogen adsorption depletes electron density from these clusters, diminishing their doping effect, thereby transmitting hydrogen adsorption events to graphene. By correlating deposition conditions, nanostructure morphology, and hydrogen sensing dynamics, our findings suggest that moderate Pt loadings can effectively balance sufficient doping with a pronounced Pt-mediated electronic response that transduces hydrogen adsorption on Pt surfaces to the Pt–graphene interface. These insights underscore the importance of combining DFT and MLIP simulations with experiments to guide next-generation chemiresistive gas sensor design.

I. INTRODUCTION

Graphene has attracted significant attention in the field of gas sensing[1–5], due to its high surface-to-volume ratio providing maximum exposure to the ambient environment, and its exceptional electronic properties such as a zero bandgap and a high carrier mobility[6,7]. Due to its zero band gap, even minute quantities of adsorbed gas molecules in its environment can induce measurable shifts in graphene's Fermi level position, and thus its conductance. The very low density of states at the Dirac point amplifies the effect of external charge donors or acceptors[4,8]. Moreover, graphene's exceptional carrier mobility ($\mu > 10^4$ cm^2/V.s) and low electrical noise facilitate the rapid detection of even subtle perturbations in its electronic structure[9,10]. Despite these remarkable features, pristine graphene often exhibits a significant limitation when utilized in gas-sensing applications; it is chemically inert, exhibiting limited binding affinity for many gas species due to its perfect honeycomb lattice of sp^2-bonded carbon atoms, which provides very few defect sites for molecular binding[11,12]. Consequently,

functionalization strategies are commonly employed to modify graphene's surface chemistry and tune its molecular binding properties[8,13,14]. One particularly effective route is to decorate graphene with metal or metal oxide nanostructures[15,16]. However, because metal oxide functionalization often suffers from limited selectivity, metal nanostructures are especially attractive[8,17]. In particular, nanostructures composed of catalytic metals such as Pt, Pd, and Ag can introduce additional active sites and promote the catalytic dissociation of specific target molecules. Moreover, both metal nanostructures and graphene exhibit excellent electron transfer properties[8]. Consequently, functionalizing graphene with catalytic metal nanostructures emerges as a highly effective strategy for enhancing sensitivity and selectivity of graphene-based gas sensors.

Among the various gaseous species of interest, hydrogen stands out owing to its extensive industrial utility in fuel cells, petrochemical refining, and ammonia synthesis[18,19]. Moreover, its pivotal significance in planetary exploration missions is underscored by its key role in atmospheric composition[20]. Furthermore, the inherent flammability of hydrogen introduces significant safety

considerations[21]. The increasing demand for fast, selective, highly sensitive, and cost-effective hydrogen sensors capable of operating near room temperature has driven extensive research into nanoengineered sensing materials[22–25]. Platinum is well known for its ability to dissociate H_2 molecules at relatively low temperatures, leading to the formation of atomic hydrogen on the metal surface[26,27]. These hydrogen atoms can either remain on the Pt clusters or, under certain conditions, spill over onto the graphene surface[28–30]. When spillover occurs, hydrogen atoms can directly alter graphene's conductivity by modifying its carrier density or introducing additional scattering sites. Even when spillover is weak or negligible, hydrogen adsorption on metal structures can still modulate the metal–graphene interface, transmitting a measurable electronic response to graphene, as investigated in this study.

Pt growth on graphene arises from a delicate interplay between cohesive Pt–Pt and interfacial Pt–C interactions[31]. Because metallic bonding is non-directional, Pt typically tends to form three-dimensional (3D) nanoclusters to maximize atomic coordination[32,33], whereas strong covalent interactions with graphene can, in principle, yield atomically thin, wetted metal layers[34,35]. Elucidating the nanoscale mechanisms governing Pt nucleation, clustering, domain coalescence, and interaction with graphene, as well as the resulting morphologies formed at various loadings and deposition rates and their influence on hydrogen reactivity, is crucial for optimizing gas-sensing performance.

A core challenge in advancing the nanoengineering of graphene–metal chemiresistive gas sensors lies in accurately modeling their thermodynamics and kinetics throughout both the crystal growth phase during sensor fabrication and the subsequent operational phase of gas detection. Although density functional theory (DFT) can provide atomistic chemical and electronic insights, it often proves computationally prohibitive for the large length and time scales required to simulate crystal growth or chemical reactivity with gases. Conversely, traditional force fields, while capable of efficiently simulating systems at these scales, often lack the precision required for these complex, multi-element, multi-structured interfaces. To address these challenges, we utilize a machine-learned interatomic potential (MLIP) based on local equivariant deep neural networks, which construct a many-body potential through iterated tensor products of learned equivariant representations[36–38]. MLIPs have recently gained prominence in computational materials science owing to their near-DFT accuracy, nearly linear scaling with system size, and excellent transferability across diverse chemical environments, with proven applications in modeling material synthesis and gas-surface interactions[39–45]. This approach guarantees both high fidelity and superior scalability when simulating complex Pt–graphene–hydrogen systems. In parallel with our computational modeling efforts, we have conducted transmission electron microscopy (TEM) and

Raman spectroscopy characterizations to examine the morphological characteristics of Pt nanostructures and their interactions with graphene at various loading levels.

In this work, we first evaluate our MLIP's accuracy in reproducing the energies and forces of diverse Pt/graphene configurations, as well as the thermodynamics of H/H_2 on Pt and graphene surfaces. We then employ the MLIP for extensive MD simulations to investigate how Pt loading and deposition rate influence crystal morphologies. Our results show that slower deposition fosters initially dispersed Pt nucleation centers, which subsequently coalesce into larger nanocluster domains closely matching experimental observations, whereas more rapid deposition can stabilize more epitaxial, one- to three-layer Pt films. The predicted structures align well with TEM data, showing predominantly polycrystalline (mainly FCC) Pt domains with random orientations and interspersed regions of exposed graphene, although higher-energy metastable phases may also arise. Finally, we explore hydrogen reactivity on the optimized Pt/graphene systems, demonstrating that at room temperature, hydrogen principally exhibits dissociative chemisorption on Pt with negligible spillover onto pristine graphene. While higher Pt coverage enhances hydrogen adsorption and uptake, it also slows dissociation/recombination kinetics. DFT-based charge-transfer analysis further indicates that undercoordinated Pt clusters induce n-type doping in graphene, but hydrogen adsorption depletes electron density from these clusters, lifting them off the graphene surface and reducing its doping level. This mechanism highlights a new hydrogen-sensing pathway mediated by Pt nanoclusters at the Pt–graphene interface, offering valuable guidance for the design of graphene–metal platforms optimized for hydrogen gas sensing.

II. RESULTS AND DISCUSSION

Benchmarking the MLIP for Modeling Pt/Graphene Structures and Reactivity to H/H_2. We initially demonstrate the generalization capabilities of our MLIP by benchmarking it against DFT calculations. Figure 1 outlines multiple aspects of this benchmarking process. Figure 1a illustrates the energies and forces predicted by the MLIP for the training structures (90%) and the unseen validation structures (10%) along with the associated error distributions. The MLIP achieves an impressive accuracy with an energy mean absolute error (MAE) less than 9 meV/atom and forces MAE below 75 meV/Å for both training and validation sets. It is noteworthy that the dataset includes a diverse array of configurations, such as Pt layered and nanocluster structures on graphene, isolated Pt clusters, and both physisorbed H_2 and chemisorbed H on various Pt/graphene configurations. This diversity is evidenced by the broad range of atomic forces and
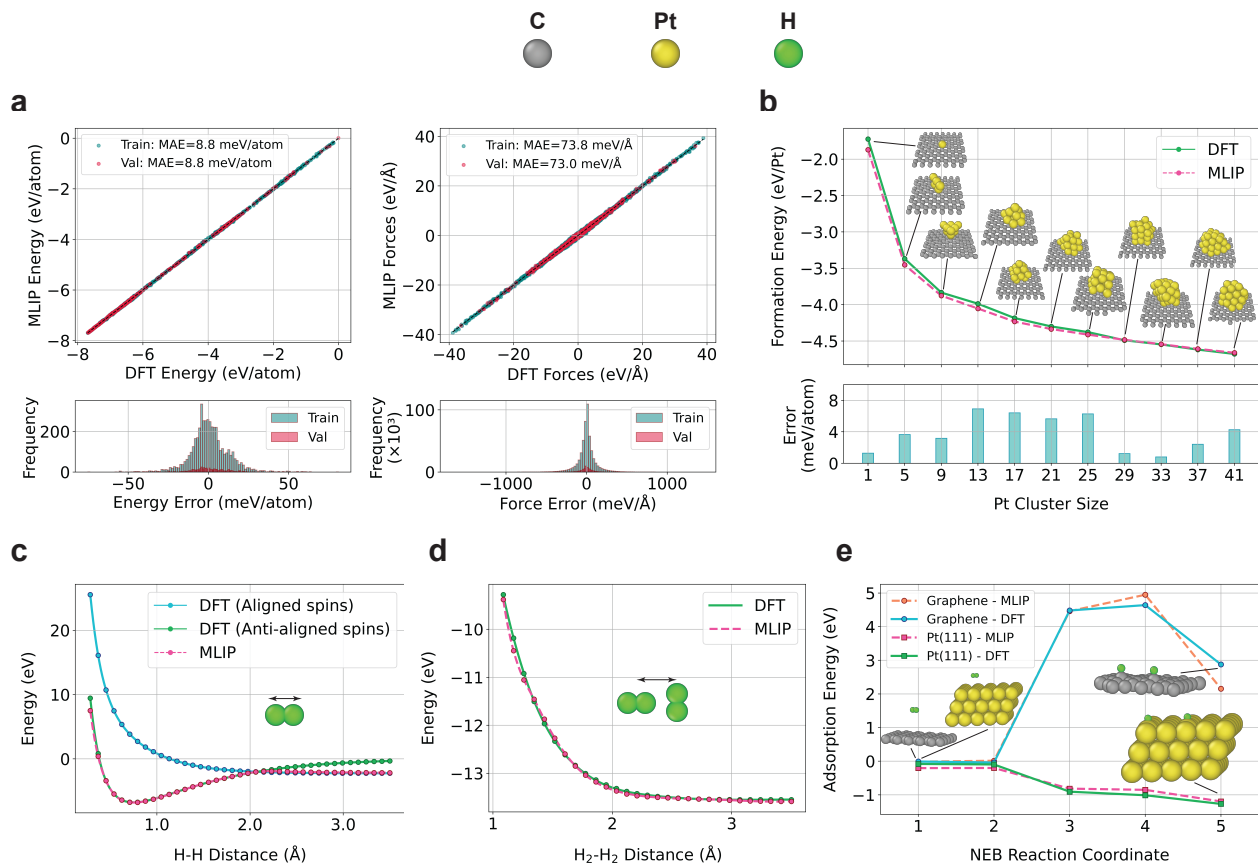
FIG. 1. **Evaluating the Machine-Learned Interatomic Potential (MLIP). a** Performance of the MLIP on the training (90%) and validation (10%) datasets for predicting DFT formation energies and atomic forces. **b** Comparison of MLIP versus DFT for predicting the formation energies (per Pt atom), along with the associated energy errors (normalized by the total number of C and Pt atoms), for Pt clusters of various sizes (optimized on graphene using the minima hopping algorithm). **c** PESs from MLIP versus DFT for H_2 molecule with aligned and anti-aligned spins. **d** MLIP versus DFT PES for two perpendicularly oriented H_2 molecules. **e** Adsorption energies from MLIP versus DFT for NEB images along the minimum energy path identified by MLIP, for H_2 dissociation on both graphene and Pt(111) surfaces.

formation energies illustrated in Figure 1a.

To further validate the predictive capabilities of the MLIP in optimizing Pt/graphene structures, we utilized the MLIP to conduct Minima Hopping (MH) optimizations. MH is a crystal structure global optimization method that utilizes a stochastic walker to traverse the potential energy surface (PES), facilitating transitions from one local minimum to another and steering the search toward more energetically favorable structures[46]. Figure 1b displays the MH-predicted configurations of Pt_N clusters on graphene for $N = 1, 5, 9, 13, 17, 21, 29, 33, 37$, and 41, alongside the corresponding formation energies as computed by the MLIP and benchmarked against DFT static calculations. The formation energy per Pt atom is defined as:

$$E_{Pt}^{form} = \left(E_{Gr+Pt}^{total} - E_{Gr}^{total} - N_{Pt} \times E_{Pt}^{vac}\right)/N_{Pt} \quad (1)$$

where E_{Gr+Pt}^{total} represents the total energy of graphene with the Pt cluster adsorbed onto it, E_{Gr}^{total} denotes the

total energy of the relaxed bare graphene without any Pt atoms, N_{Pt} is the number of Pt atoms in the cluster, and E_{Pt} refers to the energy of an isolated Pt atom in vacuum. The MLIP demonstrates high accuracy in predicting the energies of Pt clusters on graphene across various sizes, with errors less than 8 meV/atom, aligning within the established training and validation error bounds detailed in Figure 1a.

Figure 1c underscores the MLIP's accuracy in predicting hydrogen energetics by illustrating the PES for a single hydrogen molecule in two distinct spin states: aligned and anti-aligned. For H-H bond lengths exceeding ≈ 2.1 Å, the MLIP predictions closely align with the PES of aligned spins, accurately capturing the chemical dissociative limit where the hydrogen atoms are non-interacting, and no spin flipping occurs. Below this threshold, where the two PESs intersect and the H-H bond formation begins, the MLIP's predictions transition to match the anti-aligned spins PES, effectively capturing the onset of bond formation between hydrogen atoms in accordance

with the Pauli exclusion principle. Furthermore, Figure 1d displays the PES of two perpendicular hydrogen molecules, relaxed with respect to their centers of mass, as a function of the distance between these centers, demonstrating the MLIP's high accuracy in modeling the interactions between H_2 molecules in the gaseous state.

Finally, to evaluate the MLIP's capability to model the kinetics of hydrogen on both Pt and graphene surfaces, we employed the nudged elastic band (NEB) method with the climbing image technique utilizing the MLIP (see Figure 1e)[47]. The initial state featured an H_2 molecule positioned parallel to the surface at a distance exceeding 3.5 Å above the graphene and Pt(111) surfaces. The final state comprised two hydrogen atoms, each adsorbed atop two surface carbon or platinum atoms, indicative of a dissociative chemisorption state. The energies of the images along the minimum energy path connecting the initial and final states, as computed by the MLIP, were subsequently validated through static DFT calculations. The adsorption energy of hydrogen along the NEB reaction coordinate, depicted in Figure 1e, is defined as:

$$E_H^{ads} = E_{(Gr/Pt)+H}^{total} - E_{Gr/Pt}^{total} - \frac{N_H}{2} \times E_{H_2}^{vac} \qquad (2)$$

where $E_{(Gr/Pt)+H}^{total}$ is the total energy of the system comprising the graphene or platinum substrate with adsorbed hydrogen atoms, $E_{Gr/Pt}^{total}$ is the total energy of the relaxed bare graphene or platinum substrate without adsorbed hydrogen, N_H is the number of hydrogen atoms, and $E_{H_2}^{vac}$ represents the total energy of an isolated hydrogen molecule in vacuum.

Figure 1e confirms that the MLIP successfully reproduces the exothermic barrier-less dissociative chemisorption of H_2 on the Pt(111) surface[48,49]. Furthermore, the MLIP accurately captures both the endothermic dissociative adsorption of H_2 on pristine graphene and the associated high-energy barrier (~ 4.6 eV for the depicted configuration). For reference, the experimental H_2 dissociation energy in vacuum is ~ 4.5 eV[50], while DFT values on graphene can vary from ~ 3.3 to 4.7 eV depending on configuration[51].

Nucleation and Growth Dynamics of Pt on Graphene. Consider a scenario where multiple Pt atoms adsorb onto various graphene sites, initiating primary nucleations. This raises an important question: which crystal morphologies do these nascent nuclei adopt, and how do they evolve over time? To investigate this, we employ our MLIP in MD annealing simulations at 300 K for Pt depositions on graphene, providing an atomistic perspective on Pt nucleation and structural evolution under typical physical vapor deposition (PVD) conditions—where atoms are ejected from a solid source and condense onto a substrate maintained at or slightly above ambient temperature, in contrast to the higher temperatures commonly employed in chemical vapor deposition (CVD) processes[52]. Pt atoms are deposited sequentially in increments of 0.25 monolayer (ML), where one full ML

corresponds to complete coverage of the graphene substrate by a densely packed Pt overlayer, characterized by a nearest-neighbor distance of ~ 2.8 Å, consistent with the bulk interatomic spacing (see Figure S1 for details). For the depicted graphene supercell of size $60 \times 35\sqrt{3}$, 0.25 ML corresponds to 812 Pt atoms. We investigated various deposition batch sizes and found that this size (0.25 ML) sufficiently promotes the unrestricted mobility of atoms, thereby enabling them to attain ground-state configurations. Overall, we simulated Pt crystal growth with MD spanning loadings from 0.25 ML to 2.50 ML. Figure 2a illustrates the temporal evolution of Pt depositions (with a deposition batch size of 0.25 ML) on pristine graphene, showcasing three distinct loadings: 0.50 ML, 1.50 ML, and 2.50 ML. The initial frame for each loading ($t = 0$) reveals the initial random deposition of Pt atoms, equivalent to 0.25 ML, on a previously optimized loading (smaller by 0.25 ML). The different colors assigned to the Pt atoms denote the unique clusters they form upon reaching equilibrium. For instance, at a loading of 0.50 ML, the formation of 13 distinct Pt clusters at equilibrium (observed in the final temporal frame) is clearly discernible.

The MD time frames elucidate the stages of nucleation and structural evolution of Pt atoms on graphene, revealing distinct pathways for the integration of newly deposited atoms. For instance, comparing the initial frame at $t = 0$ ps and the subsequent frame at $t = 4.2$ ps for the 0.50 ML loading, one can observe two principal behaviors: some atoms aggregate to form nascent nucleating clusters—for instance, those represented by orange and violet—while others, deposited near pre-existing clusters, migrate toward and coalesce with them, enlarging their sizes, as evidenced by the green and grey clusters. These behaviors are also seen to happen concurrently where an existing cluster might attract only a fraction of the newly deposited atoms situated in its vicinity, while the remainder agglomerate into a new, separate cluster, as can be observed for the royal blue and brown clusters.

Another notable phenomenon during the nucleation stages, observed in the second time frame across all Pt loadings, is the formation of extended Pt filaments (highlighted by black oval shapes in Figure 2a). These filaments function as bridges connecting the large, previously formed Pt domains. The occurrence of these bridges escalates with increased Pt loading. From the third time frames, it becomes apparent that these filaments significantly facilitate the coalescence of the connected domains by providing a direct conduit for their agglomeration. Another mechanism of cluster coalescence can be observed in the third time frames across the 0.50 ML and 1.50 ML loadings, where clusters ranging from small to medium sizes diffuse over the graphene substrate and aggregate to form larger clusters, which are more stable with respect to their surrounding environments over relatively large MD simulation times.

Figures 2b, 2c, and 2d elucidate the temporal progression of several key properties during Pt crystal growth
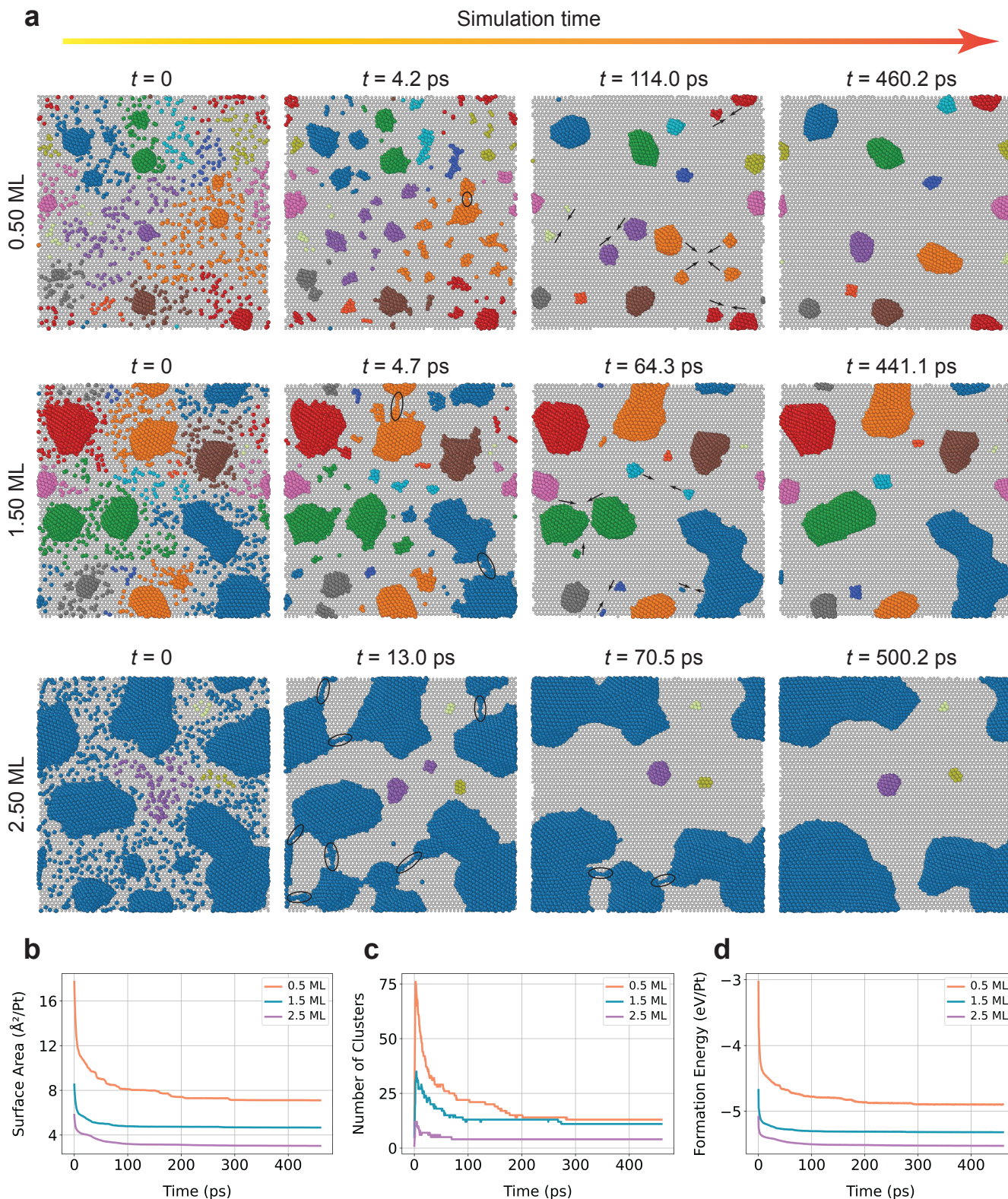
FIG. 2. **Nucleation and Structural Evolution of Pt Clusters on Graphene. a** Temporal evolution of Pt atoms on graphene, illustrated for three Pt loadings (0.50 ML, 1.50 ML, and 2.50 ML). Initial frames ($t = 0$) illustrate the baseline configuration, derived from a previously optimized structure at lower Pt loading and augmented by the stochastic deposition of a 0.25 ML batch of Pt atoms. Pt atoms are color-coded to correspond to the final cluster they inhabit. A cutoff distance of 6.5 Å is employed for clustering. **b, c, d** Trajectories of Pt surface area (per Pt atom), number of unique clusters, and formation energy (per Pt atom) over time.
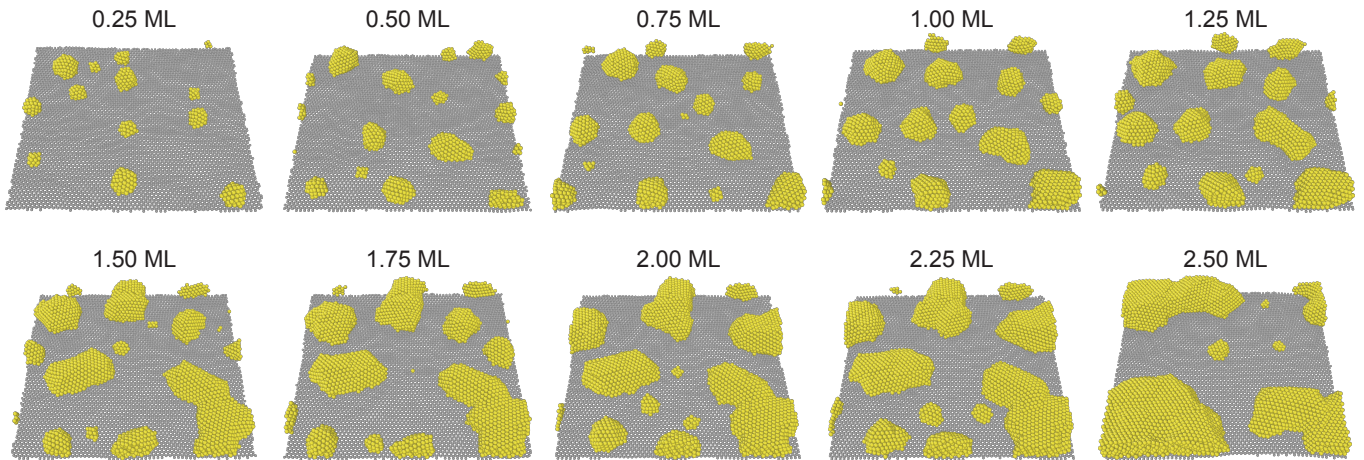
FIG. 3. **MLIP-Optimized Pt/Graphene Crystal Structures.** Optimized structures for various Pt loadings on graphene, with Pt deposited in 0.25 ML batches. The graphene cell measures 14.8 nm × 15.0 nm. MD annealing is performed in the NVT ensemble at 300 K with a 2 fs timestep, while the graphene center-of-mass velocity is zeroed.

on graphene: the surface area normalized by the number of Pt atoms, the count of Pt clusters (using Ovito's cluster analysis modifier with a cutoff distance of 6.5 Å), and the formation energy per Pt atom (Eq. 1), respectively[53]. These figures reveal a gradual decrease in these three properties over time. This trend suggests that Pt atoms, initially dispersed among numerous small clusters, progressively consolidate into fewer, larger clusters. This behavior is underpinned by a fundamental thermodynamic principle: smaller clusters, with their higher surface-to-volume ratios, exhibit elevated surface energies per atom, thereby driving the system to lower its overall free energy through cluster coalescence—a process analogous to classical coarsening[54,55].

Optimized Pt Nanostructures on Graphene. Figure 3 displays the optimized structures obtained from our MLIP-driven MD annealing simulations at 300 K for 10 different Pt loadings. The observed morphologies indicate a Volmer–Weber growth mode for Pt on graphene, characterized by the nucleation and lateral expansion of 3D islands with randomly oriented crystalline domains[56]. Both Table S1 and Figure S2 corroborate this observation, presenting statistics such as the number of clusters, cluster sizes, thicknesses, and the projected area fraction for each Pt loading. Figure S2a illustrates that, despite increased Pt planar coverage, the projected area fraction remains significantly below unity even at 2.50 ML—indicating incomplete in-plane coverage and persistent vertical stacking. For instance, at 1.00 ML, the fraction is merely 0.176, underscoring the formation of discrete 3D clusters with few-layer thickness rather than a uniform monolayer film. However, as Pt loading increases, there is a progressive, nearly linear expansion in the in-plane area of clusters, accompanied by a modest rise in cluster thickness (Figure S2b). Specifically, at lower coverages (e.g., 0.25 to 1.00 ML), the cluster

thickness ranges from 0.3 to 1.6 nm (approximately 1 to 6 or 7 Pt layers). At higher coverages up to 2.25 ML, the maximum cluster thickness does not surpass 1.9 nm (about 8 layers), and at 2.50 ML, it reaches up to 2.3 nm (about 9 or 10 layers). Observations from Figure 2 reveal that newly formed Pt nucleation sites eventually migrate via diffusion or bridging and adhere to the peripheries of pre-existing clusters. Due to this edge coalescence behavior, the vertical thickness of Pt domains (which already possess an initial few-layer stacking) displays a slowly increasing growth profile, while predominant growth is observed in the in-plane directions. This behavior aligns with our experimental observations, as evidenced by the comparative analysis of TEM Figures 6a and 6b. Furthermore, Figure 3 shows that at lower loadings, clusters maintain nearly spherical geometries but transition to more flattened morphologies at higher loadings, consistent with the changes observed in TEM analysis (Figures 6a and 6b).

From Figure S2c, it is also observed that the number of clusters remains relatively constant (between 11 and 13) for coverages ranging from 0.25 ML to 1.50 ML, but decreases to only 4 at 2.50 ML. This trend corroborates that smaller loadings are characterized by more islands of smaller sizes, and as loading increases, coupled with the lateral expansion of islands, the likelihood of these islands edge-coalescing into fewer, larger clusters also increases, since the inter-cluster distances decrease with loading, in agreement with TEM results in Figures 6a and 6b. At certain critical loadings, the inter-cluster distances may become small enough to promote significant cluster coalescence, as observed at the Pt loading of 2.50 ML, for example, as shown in Figures S2d and 2a.

Structural and Energetic Characterization of Pt Nanostructures on Graphene. Figure 4 provides further insights into the structural and energetic character-
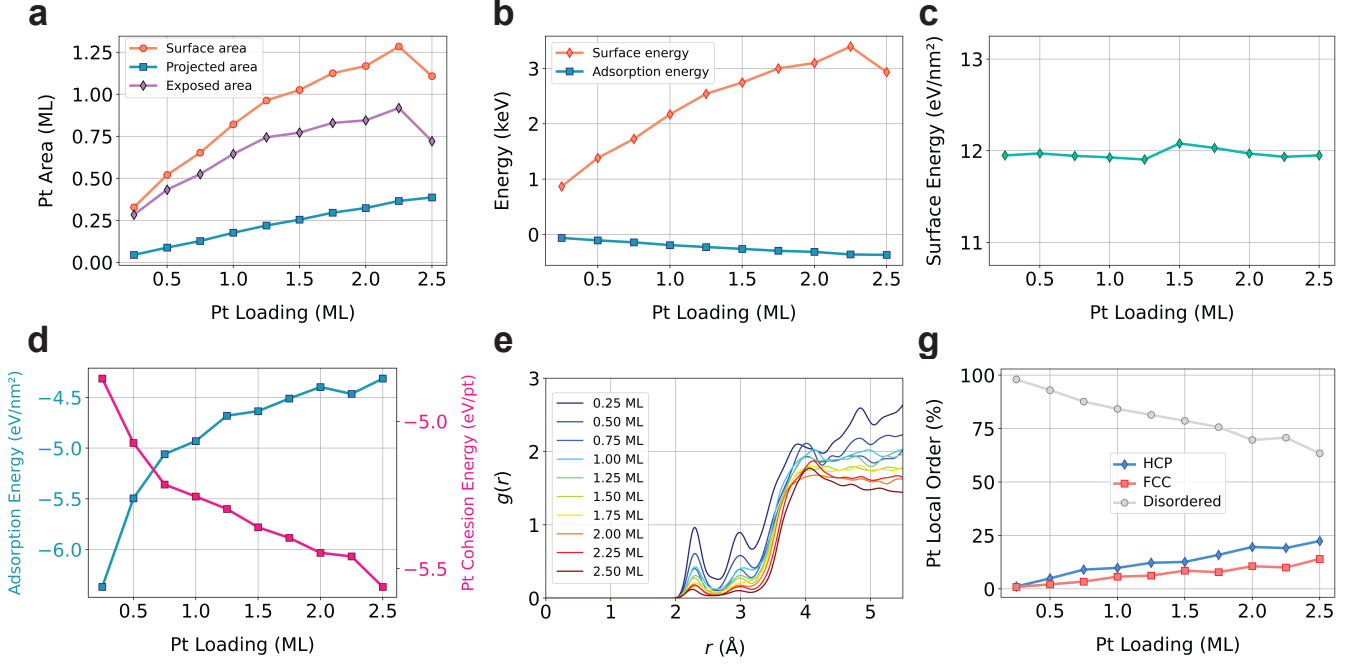
FIG. 4. **Characterization of Pt Nanostructures on Graphene.** (a) Surface area (A_{surf}), projected area (A_{proj}), and exposed area (A_{expos}) of Pt clusters versus Pt loading. (b) Surface energy of isolated Pt structures and adsorption energy of Pt on graphene as functions of Pt loading. (c) Surface energy (normalized per unit area) versus Pt loading. (d) Cohesive energy (per Pt atom) and adsorption energy (normalized by interfacial area) versus Pt loading. (e) C–Pt radial distribution function (RDF) for MD-annealed structures at various Pt loadings. (f) Distribution of local atomic environments in Pt clusters (isolated from graphene), classified as FCC, HCP, or Disordered, versus Pt loading.

istics of Pt deposits on graphene, expanding upon the morphological evolution discussed earlier. We compute three characteristic areas of Pt nanoclusters: the surface area of isolated Pt clusters (A_{surf}), assuming graphene is absent; the projected area, which delineates the footprint of Pt clusters on the graphene substrate (A_{proj}); and the exposed area of Pt that is not in direct contact with graphene ($A_{\text{expos}} = A_{\text{surf}} - A_{\text{proj}}$).

In our approach, the surface area of the 3D Pt clusters is obtained using Ovito's surface meshing modifier with the Gaussian density method[53,57]. The projected area is determined by projecting Pt atomic positions onto the xy-plane and identifying individual clusters using the Density-based Spatial Clustering of Applications with Noise (DBSCAN) algorithm[58]. An alpha-shape algorithm is then applied to each cluster to trace its boundary and compute the aggregate projected area[59].

Figure 4a illustrates how A_{surf}, A_{proj}, and A_{expos} vary with Pt loading. The projected area expands nearly linearly with Pt loading, indicative of predominant lateral domain growth accompanied by persistent vertical stacking and minimal thickening in the vertical direction, as discussed in the previous section. Conversely, both A_{surf} and A_{expos} increase at a decelerating rate, peaking around 2.25 ML before showing a small rebound at 2.50 ML loading due to the collective cluster edge-coalescence observed in Figure 2a at 2.50 ML, which leads

to a reduced proportion of Pt atoms on the free surface.

Figure 4b illustrates the evolution of surface ($E_{\text{Pt}}^{\text{surf}}$) and adsorption ($E_{\text{Pt}}^{\text{ads}}$) energies with Pt loading. The definitions used here are:

$$E_{\text{Pt}}^{\text{surf}} = E_{\text{Pt}}^{\text{total}} - N_{\text{Pt}} \times E_{\text{Pt}}^{\text{bulk}}, \tag{3}$$

$$E_{\text{Pt}}^{\text{ads}} = E_{\text{Gr+Pt}}^{\text{total}} - E_{\text{Gr}}^{\text{total}} - E_{\text{Pt}}^{\text{total}}, \tag{4}$$

where $E_{\text{Pt}}^{\text{total}}$ is the total energy of the isolated Pt nanostructure, N_{Pt} is the number of Pt atoms, $E_{\text{Pt}}^{\text{bulk}}$ is the energy per atom in bulk FCC Pt, $E_{\text{Gr+Pt}}^{\text{total}}$ is the total energy of the combined Pt/graphene system, and $E_{\text{Gr}}^{\text{total}}$ is the total energy of relaxed bare graphene.

The trend and slope of $E_{\text{Pt}}^{\text{surf}}$ mirror those of A_{surf}, with the normalized surface energy per unit area remaining relatively constant across Pt loadings, as depicted in Figure 4c. This suggests that the chemical stability of a unit surface patch of Pt remains largely unchanged with increasing loading, thereby highlighting the dominant role of surface area in governing the overall surface energy.

Figure 4b further demonstrates that $E_{\text{Pt}}^{\text{ads}}$ becomes more negative and changes in a linear fashion with Pt loading, akin to the behavior of A_{proj}. However, Figure 4d reveals that the adsorption energy per unit area becomes less negative as Pt loading increases, indicating a weakening of the local Pt–graphene interfacial binding at higher coverages. These observations together imply that while the local Pt–C bonds become weaker as

the Pt loading increases, more Pt–C bonds are formed at a higher rate, leading to an overall stronger total adsorption energy between Pt and graphene. According to the MLIP predictions in Figure 4d, the adsorption energies range from approximately -6.4 eV/nm^2 to -4.3 eV/nm^2, comparable to the binding energies reported for graphene/Pt(111)[60] (~ -4.1 eV/nm^2), with the stronger (more negative) adsorption energies at lower loadings attributed to the more undercoordinated nature of the smaller Pt nanoclusters. Overall, this range indicates relatively weak binding between Pt nanostructures and graphene, yet remains stronger than the van der Waals binding observed, for instance, between graphite layers (~ -2.0 eV/nm^2)[61].

Figure 4d shows that as Pt–graphene binding weakens, the cohesive energy per Pt atom becomes more negative—reflecting enhanced Pt–Pt interactions. This inverse relationship implies that with increasing Pt loading, local Pt–graphene interactions diminish in favor of Pt–Pt cohesion. This inverse relationship implies that with increasing Pt loading, local Pt–graphene interactions diminish in favor of Pt–Pt cohesion. Such a trend is consistent with the observed morphological evolution in which small domains grow into larger ones through the incorporation of newly deposited Pt atoms or via cluster coalescence, ultimately resulting in a higher fraction of bulk-like interior atoms relative to surface or interfacial atoms.

Figure 4e further corroborates these trends by depicting the C–Pt radial distribution function (RDF), which exhibits distinct peaks at approximately 2.3 Å, 3.0 Å, and 4.1 Å. Notably, our DFT calculations indicate that the C–Pt bond length for a Pt adatom on graphene in the dilute regime is ~ 2.1 Å (at bridge site), closely aligning with the first peak of the C–Pt RDF predicted by the MLIP across various Pt loadings; however, for these higher loadings, the first peak is expected to shift to a slightly larger bond length (2.3 Å) compared to that of a single adatom. As Pt loading rises, the population of Pt atoms located close to the graphene surface at the first two peaks gradually decreases, while an increasing number of Pt atoms become partially or fully screened at larger distances. This screening mechanism accounts for the weaker local interfacial binding observed in Figure 4d. Although some Pt atoms remain anchored within 3 Å of the graphene surface across all loadings, the overall trend indicates that enhanced Pt–Pt cohesion at higher loadings attenuates the local Pt–graphene binding.

Lastly, Figure 4g employs the polyhedral template matching algorithm in Ovito[53,62], with a root-mean-square deviation (RMSD) threshold of 0.12, to classify the atomic environments within the Pt clusters based on coordination. Atomic environments are categorized as hexagonal close-packed (HCP), face-centered cubic (FCC), or "Disordered"—the latter denoting configurations that do not conform to any crystallographic template in the algorithm's reference set (including FCC, HCP, body-centered cubic, icosahedral, simple cubic,

cubic diamond, or hexagonal diamond). Figure 4g shows that with increasing Pt loading, the fraction of disordered environments diminishes in favor of FCC and HCP orderings. This trend highlights the crystallographic heterogeneity of small Pt clusters, where high surface-to-volume ratios promote less-ordered arrangements; as clusters grow, surface effects diminish and crystalline FCC/HCP configurations emerge. Our DFT calculations indicate that the energy difference between bulk FCC and HCP stacking in Pt is ~ 53 meV/atom (with FCC more stable), decreasing to ~ 31 meV/atom for six-layer [111]-like slabs and further to ~ 6 meV/atom for three-layer slabs. Consequently, at the nanoscale, FCC and HCP phases become nearly degenerate, permitting the coexistence of multiple stacking orders at typical simulation temperatures (300 K ~ 26 meV). Moreover, it is worth noting that the polyhedral template matching method employed in Figure 4g identifies only bulk-like atomic environments closely matching ideal FCC or HCP geometries; hence, Pt atoms at surfaces or cluster edges are not classified as FCC or HCP, even though they could adopt such stacking if incorporated into bulk-like regions.

Epitaxial Pt on Graphene. In the preceding sections, we demonstrated that slower, sequential Pt deposition promotes energetically stable morphologies, predominantly forming 3D nanoclusters that grow in-plane and coalesce into larger islands with increasing Pt loading. In contrast, we now investigate the potential stabilization of two-dimensional (2D) epitaxial Pt arrangements under a higher effective deposition rate. For this purpose, we selected the 2.00 ML loading as a case study. To simulate the extreme limit of rapid deposition, the entire Pt loading was introduced in a single batch. We also explored an intermediate scenario by sequentially depositing 1.00 ML (as opposed to the previously used 0.25 ML); however, the resulting morphology was similar to that produced by a single-batch deposition. Figure 5 illustrates the annealed structure resulting from the rapid deposition of a 2.00 ML Pt loading. Notably, this process stabilizes thin Pt films—typically up to three layers thick—that contrast sharply with the 3D nanocluster morphology by covering a larger fraction of the graphene substrate and predominantly forming monolayer (ML), bilayer (BL), and trilayer (TL) domains. This epitaxial growth of Pt thin films (1–3 layers) on graphene has been demonstrated experimentally[34,63].

The stabilization of these thin films arises from the limited mobility of Pt atoms under a high effective deposition rate. Under rapid deposition conditions, most newly deposited Pt atoms immediately encounter a dense local environment, which severely restricts their mobility and drives the formation of a single, large epitaxial domain. This behavior can be interpreted through the lens of percolation theory, in which, once a critical density is surpassed, a geometric phase transition occurs such that the formation of new, disconnected clusters becomes negligible and a single connected cluster
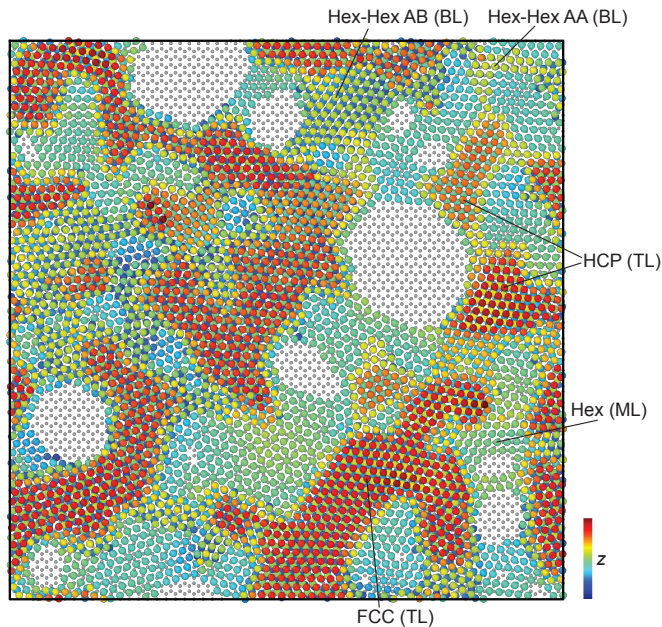
FIG. 5. **MLIP-Optimized Epitaxial Pt/Graphene Crystal Structure.** Final configuration from MD annealing following a rapid, single-batch deposition of 2.00 ML Pt on graphene. The color map indicates the z-coordinate of the Pt atoms.

TABLE I. Key structural and energetic properties of Pt on graphene at a 2.00 ML loading, comparing slow deposition (3D nanocluster) and fast deposition (2D epitaxial thin film).

Deposition mode	Slow	Fast
Pt morphology	nanoclusters	thin film
Surface Area (ML)	1.17	1.95
Projected Area (ML)	0.32	0.93
Exposed Area (ML)	0.85	1.02
Formation Energy (eV/Pt)	-5.49	-5.27
Pt Surface Energy (keV)	3.10	4.88
Graphene/Pt Surface Energy (keV)	2.78	4.26
Adsorption Energy (keV)	-0.32	-0.63
Adsorption Energy (eV/nm^2)	-4.40	-3.05

emerges[64]. Furthermore, during MD annealing, as the thin film minimizes its surface area, isolated interior regions of exposed graphene emerge. This duality in the growth regimes—where slow deposition produces multiple, spatially separated Pt clusters on a largely exposed substrate, while rapid deposition yields a nearly continuous film interspersed with small, uncovered graphene patches—exemplifies a yin–yang behavior in Pt growth modes on graphene.

Table I compares the thin film with its 3D nanocluster counterpart. The 2D configuration covers nearly 3 times the projected area of the nanoclusters. Although the 2D film exhibits a higher (i.e., less negative) formation energy and is therefore less stable, it provides about 1.2 times more Pt-exposed area, indicating a moderate increase in accessible surface sites and a correspondingly

higher surface energy. Moreover, while the overall adsorption energy on graphene is more negative for the 2D film, normalization by the projected area reveals an approximately 30% lower adsorption energy per unit area, suggesting that despite covering a larger portion of the substrate, the 2D film forms weaker local Pt–graphene interactions.

Further structural insights are provided in Figure 5, where Pt atoms adsorb onto the graphene substrate, forming incommensurate domains due to lattice mismatch (graphene: 2.47 Å; bulk Pt–Pt: 2.81 Å). Nevertheless, Pt atoms predominantly occupy nearby bridge sites on graphene, consistent with our DFT results that rank bridge, top, and hollow sites in order of decreasing energetic favorability. In ML regions, the most stable arrangement is a close-packed hexagonal configuration; BL regions maintain a hexagonal in-plane structure with either AA or AB stacking, while TL regions adopt FCC- or HCP-like sequences, in line with the small DFT-predicted energy difference (~ 6 meV/atom) between these stacking modes.

To further investigate the preferred atomic coordination in 2D Pt domains, we performed DFT calculations for various free-standing BL models. Table S2 and Figure S3 summarize these structures classified by their in-plane lattice symmetry—square (sq) or hexagonal (hex)—and by their second-layer stacking orientation (top, center, or bridge). Among the square configurations, the sq–sq-top model yields a cohesive energy of -4.86 eV/atom, while sq–sq-center is slightly more stable at -4.95 eV/atom. These square domains, possessing relatively higher energies, are considered metastable and may become kinetically trapped during rapid condensation on cooler substrates in the electron-beam PVD process (as further discussed in the TEM analysis in the following section). In contrast, hexagonal configurations exhibit stronger cohesive energies of approximately -5.19 eV/atom across hex–hex-top, hex–hex-bridge, and hex–hex-center arrangements, with the hex–hex-center stacking being marginally more stable. These findings are consistent with the MLIP-driven annealing results in Figure 5, which show that BL regions adopt either hex–hex-top (AA) or hex–hex-bridge (AB) arrangements, while hex–hex-center stacking is absent due to its tendency to nucleate a third layer, transitioning toward an FCC- or HCP-like TL configuration.

TEM Characterization and Analysis. The Pt functionalization was performed using electron-beam PVD, as described in the "Methods" section. Prior to deposition, an outgassing step was carried out to remove any native oxide or surface contaminants, ensuring a clean Pt deposition process. During deposition, the Pt film thickness was monitored using a crystal monitor for precise control over film growth. Due to the relatively fast film growth rate, two different deposition times were selected: 1.5 and 3.0 minutes, depositing approximately 0.4 nm and 1.0 nm of Pt on graphene, respectively. These
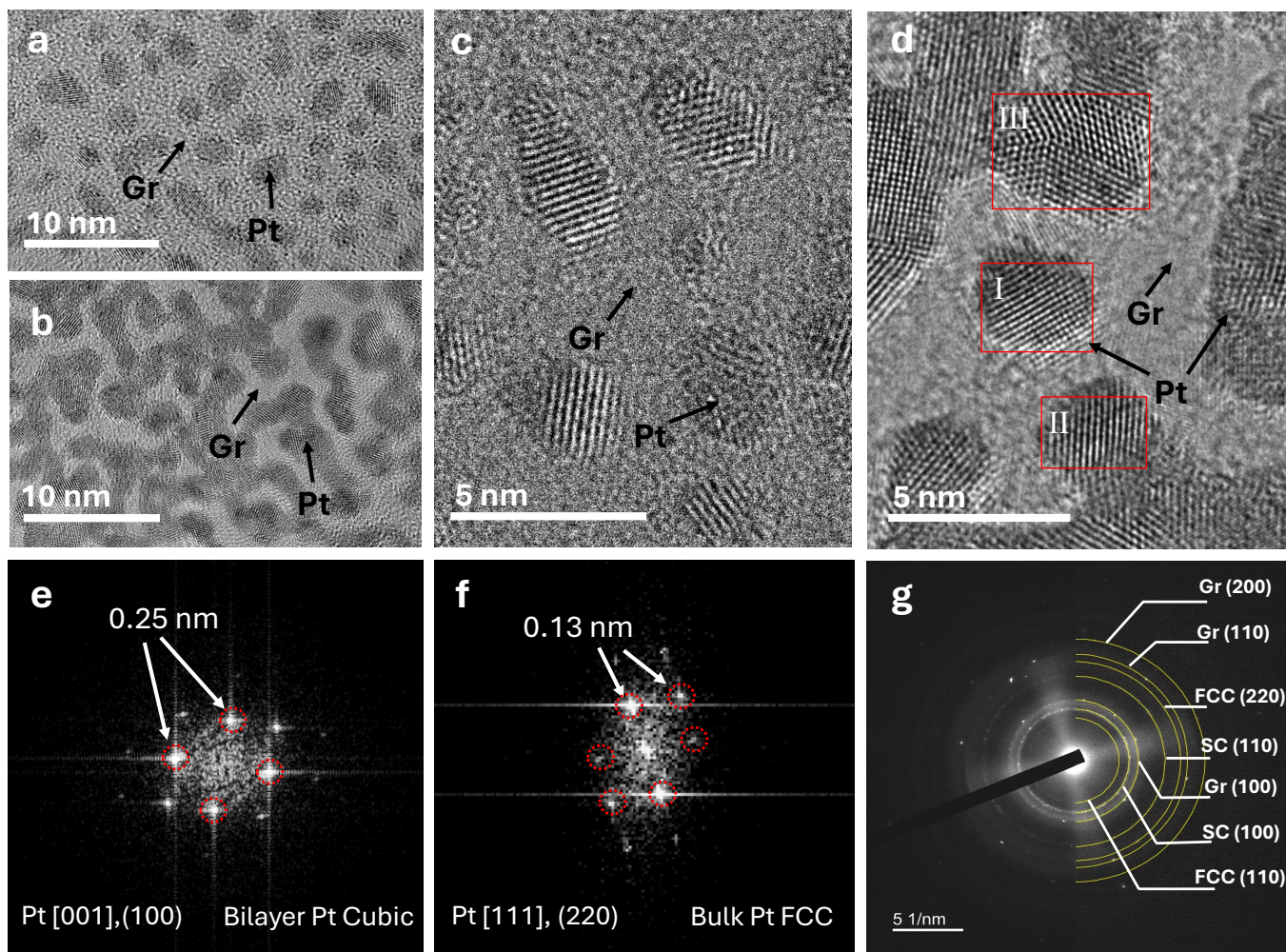
FIG. 6. **TEM Characterization of Pt Structures on Graphene.** TEM and HRTEM images at 1.5 minutes (a, c) and 3 minutes (b, d) of deposition are shown. **(e)** FFT analysis for region I, showing a cubic crystal structure viewed along the [001] axis. **(f)** FFT analysis for region III, showing an FCC crystal structure viewed along the [111] axis. **(g)** SAED pattern for Pt on graphene after 3 minutes of deposition.

conditions resulted in two distinct surface morphologies, allowing for the tracking of film growth.

To investigate possible structural changes in graphene following Pt deposition, Raman characterization was performed before and after deposition. As shown in Figure S6, both the 1.5-minute and 3.0-minute Pt depositions produce no significant shifts in the G (1580 cm^{-1}) or 2D (2700 cm^{-1}) peaks. Likewise, their intensity ratio (I_{2D}/I_G) remains approximately unchanged. This indicates that the graphene lattice remains essentially intact and that the Pt deposition process does not induce significant lattice disorder or strong doping sufficient to substantially shift the Fermi level. However, it is worth noting that the G band exhibits slight broadening in both samples, with more pronounced broadening observed for the larger Pt loading. This behavior points to localized charge interactions between Pt nanostructures and graphene[65], which is corroborated by our MLIP-driven MD simulations that show an increased Pt–graphene in-

terface area and a larger total adsorption energy as the Pt loading increases (see Figures 4a, 4b). Since the G band is highly sensitive to in-plane stretching of C–C bonds in sp^2 carbon, its broadening additionally suggests localized strain induced by Pt clustering on the graphene surface. This inference is supported by our MD simulations, which show that graphene develops ripples beneath the growing Pt clusters (Figure 3). Meanwhile, the D peak at approximately 1350 cm^{-1} shows a small increase in intensity, indicating minor localized defects or lattice disruptions[66]. However, the modest magnitude of this D peak change confirms that Pt deposition introduces only minimal defects to graphene. Collectively, these findings highlight that Pt functionalization induces moderate local strain and charge interactions with graphene, yet the overall integrity of the graphene film remains well preserved, with minimal disorder or defects.

High-resolution TEM (HRTEM) was used to characterize the structural properties of Pt-functionalized

graphene. As shown in Figure 6a, after 1.5 minutes of deposition ($\sim$ 0.4 nm), the deposited Pt forms sparse, isolated nanoclusters dispersed on the graphene surface. Figure 6c presents a higher-magnification image of these Pt clusters, in good agreement with our MLIP results that predict small, nearly spherical Pt nanoclusters at lower Pt loadings (see Figure 3). Based on Raman analysis (Figure S6), these small clusters do not significantly disrupt the graphene lattice. As deposition proceeds to 3 minutes ($\sim$ 1.0 nm) (Figure 6b), the Pt film develops larger and more closely spaced domains, where the smaller Pt clusters tend to coalesce laterally, merging into larger Pt aggregates that reduce the exposed graphene area, again in line with MLIP predictions (see Figure 3).

Three distinct Pt regions appear in the higher-magnification image of the 1.0 nm loading (Figure 6d), highlighted by boxes (I), (II), and (III). In region (I), a relatively thin Pt domain lies on top of graphene. Fast Fourier transform (FFT) analysis for this region reveals a set of reflections consistent with a simple cubic (SC) crystal structure, viewed along the [001] direction, exhibiting (100) reflections at 0.25 nm (Figure 6e). According to previous reports[34,67], such SC characteristics have been attributed to the formation of a Pt bilayer on graphene. However, our DFT calculations (Table S2 and Figure S3) indicate that the SC phase is less energetically favorable than other hexagonal arrangements. The formation of these metastable SC domains may result from the non-equilibrium nature of electron-beam PVD, which rapidly condenses vapor metal atoms on a cooler substrate under conditions that may lack sufficient surface mobility to relax into more stable phases, such as the FCC phase for Pt[68]. In contrast, for Pt domains with higher mobility on graphene, Pt typically adopts a [111] surface parallel to the graphene plane to match its hexagonal symmetry, consistent with our MLIP predictions (see Figure 5).

In region (II), a thicker Pt layer is observed. Based on FFT analysis, this region exhibits an FCC crystal structure viewed along the [111] direction, with (220) reflections at 0.13 nm (Figure 6f). The formation of the FCC phase here is primarily attributed to the increased atomic mobility of Pt atoms as the film thickens[69]. As Pt domains grow, upper atoms become more effectively shielded from direct contact with graphene (no longer pinned by the Pt–graphene interface), diminishing the substrate's influence relative to the Pt–Pt cohesive interactions that begin to dominate within the domain interior. Since FCC represents the global minimum-energy configuration for bulk platinum, these thicker regions tend to relax into the FCC phase. This is consistent with the MLIP-driven MD results shown in Figure 4g. Lastly, region (III) exhibits FCC Pt domains with various orientations that merge into larger clusters, in agreement with MLIP predictions for the cluster coalescence process (Figure 2).

To further investigate the crystal structure of the deposited Pt over a larger area, selected area electron diffraction (SAED) was performed following HRTEM and FFT analysis. As shown in Figure 6g, the diffraction rings confirm that the Pt clusters exhibit a polycrystalline structure with randomly oriented crystalline domains, in agreement with the MLIP predictions (Figure 3). By analyzing the interplanar spacings (Table S3), we identified reflections corresponding to both FCC and SC phases of Pt. The SAED pattern (Figure 6g) shows reflections from FCC (220) (at 0.13 nm), consistent with the FFT analysis (Figure 6f). Additionally, reflections from SC (100) (at 0.25 nm) and SC (110) (at 0.15 nm) align with FFT analysis (Figure 6e) and previous findings for bilayer Pt on graphene[34]. For the DFT bilayer structures considered in Table S2 and Figure S3, we find that the SC bilayer (sq-sq-top) exhibits (100) spacing of roughly 0.25 nm, in agreement with the experimental value. However, while the theoretical value expected for the (110) spacing should be $0.25/\sqrt{2} \approx 0.178$ nm, we attribute the discrepancy to minor possible distortions in the in-plane direction. This argument is bolstered by the energetic favorability of hexagonally ordered Pt configurations, as noted in Table S2. Indeed, a small distortion of about 6 degrees can reduce the (110) spacing from 0.178 nm to approximately 0.15 nm. Furthermore, reflections with a 0.31 nm spacing are observed, which are close to the Pt FCC (110) spacing of 0.28 nm. We suggest that this slight discrepancy results from a distortion of the Pt FCC lattice induced by the underlying hexagonal graphene substrate. The strain evidence inferred from Raman measurements, the graphene rippling observed in MD simulations, and the identification of potential stacking faults in FCC Pt nanostructures (manifesting as HCP domains in MD) collectively reinforce the likelihood of such distorted Pt FCC arrangement. Finally, the SAED pattern exhibits well-defined hexagonal graphene diffraction spots, further confirming that the structural integrity of graphene was preserved throughout the deposition process without introducing significant damage or defects, as also indicated by Raman measurements.

These TEM findings provide valuable insights into the growth behavior of Pt on graphene, highlighting the coexistence of different Pt phases and the formation of polycrystalline Pt domains, in agreement with our computational predictions.

Hydrogen Reactivity on Pt/Graphene Structures. To investigate the reactivity of hydrogen with Pt/graphene nanostructures, we conducted reactive MD simulations at 300 K with 1200 H_2 gas molecules, for the optimized Pt/graphene crystal structures at loadings of 0.50 ML, 1.00 ML, 1.50 ML, 2.00 ML, 2.25 ML, and 2.50 ML. In the initial configuration, we strategically position the H_2 molecules within a region from 5 to 20 Å above the highest atom in the Pt/graphene structure, ensuring no direct initial contact. The simulation employs periodic boundaries in the lateral directions and incorporates a rigid wall approximately 6 nm above the graphene sheet, serving as a reflecting barrier for the H_2 molecules. To mitigate the nonphysical drift that may arise from the
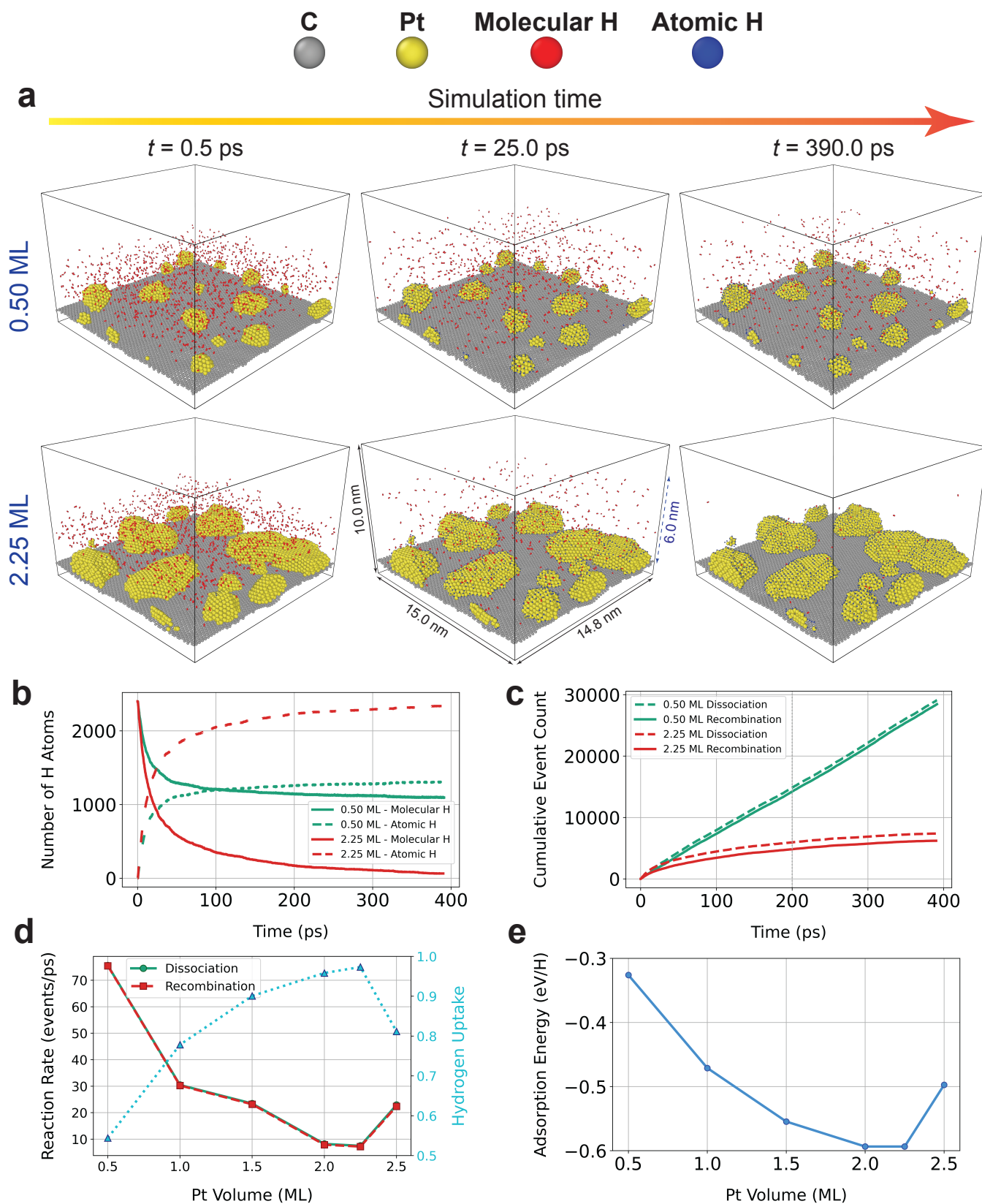
FIG. 7. **Hydrogen Reactivity on Pt/Graphene Structures.** (a) Temporal evolution of 1200 H_2 molecules interacting with optimized Pt/graphene structures at two Pt loadings (0.50 ML and 2.25 ML), at 300 K with a 1 fs MD timestep. (b) Evolution of the number of hydrogen atoms in molecular (H_2) and atomic (2H) states, determined by coordination (1 or 0) within a 1.0 Å cutoff (for the 0.50 ML and 2.25 ML loadings). (c) Cumulative counts of dissociation ($H_2 \rightarrow 2H$) and recombination ($2H \rightarrow H_2$) events over time (for the 0.50 ML and 2.25 ML loadings). (d) Reaction rates and hydrogen uptake (fraction of captured H) as a function of Pt loading. (e) Adsorption energies of hydrogen (per H atom) at 390.0 ps for various Pt loadings.

unrealistically high initial partial pressure of H_2 used in simulations ($\sim$ 37 bar), we nullify the net linear momentum of the graphene substrate and the center-of-mass momentum of each Pt cluster. This elevated initial H_2 pressure ensures a larger ensemble of H_2 molecules, enabling clearer trends to be drawn regarding the chemical reaction events, as demonstrated in previous studies[43,44].

Figure 7a shows the dynamics of hydrogen interacting with Pt/graphene at two loadings (0.50 ML and 2.25 ML). Within 0.5 ps, the H_2 gas disperses uniformly throughout the simulation box. Over time, the molecular hydrogen (H_2, shown in red) interacts primarily with the Pt clusters, undergoing dissociative chemisorption and converting into atomic hydrogen (H, shown in blue). Interestingly, the simulations indicate that hydrogen exhibits negligible direct interaction with pristine graphene. Note that our Raman analysis (Figure S6) reveals that defect levels are minimal in graphene, justifying the assumption of pristine graphene in our simulations. Under standard conditions, unfunctionalized graphene is known to be chemically inert to H_2, with a high dissociation barrier (approximately 3.3 eV)[51]. However, the absence of significant H–graphene interaction even after Pt functionalization—which provides active sites for H_2 dissociation—suggests that H spillover from Pt clusters to pristine graphene is negligible. The binding energy of a single H adatom on graphene (at the top site) is -0.9 eV according to our DFT (PBE+D3) calculations, in agreement with previous studies, and is slightly overestimated by our MLIP at -1.19 eV[70]. These results indicate that H adsorption on graphene is exothermic according to both MLIP and DFT, ruling out any potential MLIP bias that might underestimate the energetic favorability of H adsorption on graphene and, consequently, erroneously reduce H spillover. In fact, the absence of H spillover can be attributed to the relatively weak Pt–graphene coupling, as confirmed by our Raman spectroscopy and MLIP predictions (Figure S6 and 4d). This weak coupling allows Pt nanoclusters to form stronger H–Pt bonds (see Figure 7e)—likely due to enhanced electron density at the Pt sites that stabilizes the chemisorbed hydrogen—thereby increasing the barrier for H atoms to desorb from Pt clusters and migrate to adsorb onto the graphene lattice. Prior studies support this hypothesis, demonstrating that stronger metal–substrate interactions facilitate H spillover[28,29,71]. Other studies also show that the H spillover barrier from Pt clusters to pristine graphite is very high (> 50 kcal/mol)[30]. Although hydrogen primarily adsorbs on Pt, these adsorption events can still induce bonding perturbations detectable at the Pt–graphene interface, providing a sensing channel distinct from a direct H–graphene interaction, as detailed in the following sections.

Figures 7b and 7c quantify hydrogen capture and reactivity over time for Pt loadings of 0.50 ML and 2.25 ML. Each hydrogen atom is classified as either atomic (H) or molecular (H_2) based on its coordination number (considering only neighboring H atoms) within a 1.0 Å

cutoff, with 0 indicating an atomic state and 1 indicating a molecular state. Figure 7b shows an exponential increase in atomic hydrogen and a corresponding decrease in molecular hydrogen during the first 100–200 ps, followed by roughly constant amounts at later times close to 400 ps. Figure 7c depicts the cumulative dissociation ($H_2 \rightarrow 2H$) and recombination ($2H \rightarrow H_2$) events, monitored every 50 fs, with reaction rates determined from the slopes after a 200 ps equilibration period. Together, these figures indicate that the amount of chemisorbed hydrogen is significantly higher at 2.25 ML than at 0.50 ML, while the reaction rate is notably lower at the higher Pt loading.

Extending the analysis across all Pt loadings, Figure 7d presents the hydrogen uptake (fraction of captured hydrogen atoms) and the equilibrium reaction rates for six Pt loadings; reaction rates normalized per Pt atom and per unit exposed Pt area are provided in Figure S4 for reference. Notably, hydrogen uptake increases with Pt loading at a diminishing rate, peaking at 2.25 ML before declining at 2.50 ML (due to the collective cluster coalescence at 2.50 ML loading). This trend mirrors the behavior of the exposed/surface areas and surface energy shown in Figures 4a and 4b, suggesting that the increased hydrogen uptake results from a larger number of active sites for hydrogen dissociation and adsorption on Pt surfaces. In addition, the hydrogen adsorption energy curve versus Pt loading (Figure 7e) inversely correlates with the hydrogen uptake trend in Figure 7d, indicating that stronger adsorption enhances hydrogen retention and increases the amount of captured hydrogen.

Furthermore, Figure 7d shows that the equilibrium reaction rates decrease rapidly with increasing Pt loading, reaching a minimum at 2.25 ML before rising again at 2.50 ML (due to the collective cluster coalescence at 2.50 ML loading). This pattern mirrors the trend in hydrogen adsorption energy on the Pt/graphene structures (Figure 7e), indicating that the reaction rate is primarily governed by adsorption energy. This suggests that there is no significant barrier or activation energy for H_2 dissociative chemisorption on these Pt cluster surfaces—akin to the barrierless hydrogen adsorption observed on the Pt(111) surface (Figure 1e) and reported for small Pt clusters[29,30]. Stronger adsorption correlates with a reduced desorption rate, which lowers the recombination rate of desorbed H atoms and limits the availability of unhydrogenated Pt sites for hosting H_2 dissociative chemisorption events over time. This correlation explains the proportional trends observed between the reaction rates and the adsorption energy in Figures 7d and 7e.

In addition, the MLIP-calculated adsorption energies fall within the U.S. Department of Energy's recommended range of -0.20 to -0.80 eV/H for optimal efficiency in solid-state hydrogen storage[72]. This moderate binding energy benefits sensor functionality by allowing effective hydrogen capture while ensuring rapid desorption for prompt recovery.

In chemiresistive gas sensing, surface reaction rates largely determine the response and recovery times. Our simulations show that lower Pt loadings yield smaller nanoclusters with faster kinetics (Figure 7d), resulting in shorter response times, whereas higher Pt loadings lead to stronger hydrogen adsorption that slows kinetics and may extend recovery times.

Another key factor in optimizing a gas sensor is its sensitivity, which in this case is largely governed by charge interactions at both the Pt–graphene and H–Pt interfaces. These interactions can be qualitatively assessed through the MLIP-calculated normalized adsorption energies. Our MD simulations confirm that hydrogen predominantly interacts with Pt, with negligible spillover onto pristine graphene. On one hand, the calculated normalized adsorption energies indicate that H–Pt binding generally strengthens with increasing Pt loading (Figure 7e), suggesting enhanced hydrogen sensing at the active Pt sites. On the other hand, increased Pt–Pt cohesion at higher loadings weakens local Pt–graphene interactions (Figure 4d), potentially attenuating the signal transmitted from hydrogen adsorption events on the Pt surfaces to the Pt–graphene interface. Additionally, thicker Pt nanoclusters at higher loadings may screen the H–Pt perturbations, further attenuating their influence on the Pt–graphene interface. Thus, while higher Pt loadings may enhance the sensing of hydrogen adsorption at Pt surfaces, lower Pt loadings can provide less shielding and enable better signal transmission to the Pt–graphene interface. Nevertheless, sufficient Pt coverage is also essential to achieve adequate doping and maintain a stable baseline conduction path, thereby avoiding inconsistent or noisy signals. As shown in Figures 4a and 4b, as loading increases, the greater number of Pt–C bonds compensates for the weakened local Pt–graphene binding, and the overall absolute adsorption energy increases, suggesting enhanced graphene doping. An optimal Pt loading must therefore balance these competing factors to maximize sensitivity in Pt-functionalized graphene gas sensors.

Charge Transfer and Bonding in Pt–Graphene Structures. We performed DFT (PBE) calculations on a range of bare Pt nanostructures on graphene to investigate how undercoordinated Pt modifies graphene's electronic properties. Table II summarizes the work functions on the graphene-facing side (i.e., the side opposite to adsorption), ϕ, together with the vertical Pt–graphene separations, $\Delta z_{Gr-Pt_{min}}$. We considered single Pt adatoms and vertically oriented Pt dimers at various supercell sizes, along with two larger nanoclusters, Pt_9 and Pt_{17}. A four-layer Pt(111) slab on graphene (as modeled in[73]) is also included as a representative of thicker, continuous, bulk-like metallic films. Our DFT calculations yield a work function for pristine graphene of $\phi_{Gr} = 4.62$ eV, in close agreement with the experimental value of 4.56 eV[74].

As detailed in Table II, all considered finite Pt nanos-

TABLE II. DFT (PBE) calculations for various Pt structures on graphene. Columns list the Pt structure and the associated graphene supercell size, the work function on the graphene-facing side (ϕ) along with its deviation from pristine graphene ($\phi_{Gr} = 4.62$ eV with PBE), and the vertical Pt–graphene separation ($\Delta z_{Gr-Pt_{min}}$).

Pt structure (supercell size)	ϕ (eV)	$\Delta z_{Gr-Pt_{min}}$ (Å)
Pt Adatom		
2×2	4.34 (-0.28)	2.09
3×3	4.14 (-0.48)	2.16
4×4	4.34 (-0.28)	2.22
5×5	4.42 (-0.20)	2.26
Pt Dimer		
2×2	4.30 (-0.32)	2.16
3×3	4.26 (-0.36)	2.23
4×4	4.40 (-0.22)	2.28
5×5	4.46 (-0.16)	2.30
Pt_9 Nanocluster		
5×5	4.35 (-0.27)	2.40
Pt_{17} Nanocluster		
6×6	4.30 (-0.32)	2.38
Pt(111) Slab		
2×2	4.68 (+0.06)	3.88

tructures (adatoms, dimers, and nanoclusters) exhibit work functions below 4.62 eV, indicating n-type doping of graphene by undercoordinated Pt. In contrast, only the continuous, thick slab shows a modest p-type doping with a work function of ~ 4.68 eV, consistent with the higher intrinsic work function of bulk Pt(111) that typically induces p-type doping in graphene[73,75]. This distinction between finite Pt nanoclusters and extended metallic slabs is largely driven by the undercoordination of Pt in small clusters [76–78]. Without the full coordination environment of bulk metal, the valence electron energy levels in these clusters are less stabilized, which shifts their Fermi level upward relative to the vacuum level. Consequently, these Pt nanostructures are more prone to donate charge to graphene—whose Dirac point lies at lower energy—rather than withdrawing electrons, as occurs at a bulk-Pt/Gr interface[76,77].

Figure 8 supports these conclusions by displaying charge-density difference plots for three representative Pt–graphene systems: the Pt_9 nanocluster, the Pt_{17} nanocluster, and the four-layer Pt(111) slab. In both nanocluster cases, the isosurfaces show that, in the C–Pt bonding region, electron density accumulates near the graphene layer while depletion occurs at the lower Pt atoms, highlighting a net electron transfer from these Pt atoms to graphene. In contrast, the Pt(111) slab exhibits electron depletion closer to graphene and accumulation near the slab, consistent with bulk Pt extracting electrons from graphene and inducing p-type doping[73,75].

Table II further reveals that increasing the Pt lateral coverage in both the adatom and dimer series—from a 5×5 to a 3×3 supercell—lowers the work function
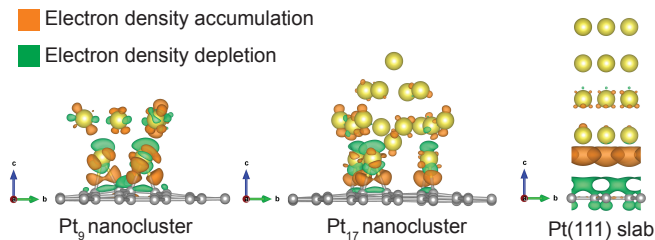
FIG. 8. **Charge Density Difference.** The figure shows charge density differences for three Pt/graphene configurations: Pt_9 and Pt_{17} nanoclusters, and a four-layer Pt(111) slab. Orange isosurfaces indicate electron accumulation, while green denotes electron depletion. Isosurface values are 0.005 $e/\text{Å}^3$ for the nanoclusters and 0.0003 $e/\text{Å}^3$ for the slab.

relative to pristine graphene ($\phi_{\text{Gr}} = 4.62\,\text{eV}$) more significantly and reduces the vertical Pt–graphene separation. These trends are consistent with stronger Pt-graphene bonding and enhanced electron transfer from Pt to graphene. However, when the coverage is pushed to the 2×2 supercell size limit, the work function partially rebounds rather than decreasing further, suggesting that strong lateral Pt–Pt cohesion inhibits additional charge transfer. Similarly, vertically oriented Pt dimers generally exhibit a smaller drop in the work function relative to ϕ_{Gr} compared to single Pt adatoms, indicating that vertical growth also moderates electron donation from Pt to graphene. This outcome is consistent with our MLIP-based observations, which show that as Pt loading increases and domains become thicker and more cohesive, enhanced Pt–Pt interactions weaken the local Pt–graphene interfacial binding, as illustrated in Figure 4d.

Hydrogen Sensing at the Pt–Graphene Interface. Chemiresistive gas sensing in graphene-based sensors relies on the modulation of graphene's electrical resistance, induced by changes in its carrier concentration or mobility upon exposure to the target gas.

Figure S5 displays the time-resolved average Pt–C distance, calculated by considering Pt atoms within a 6.5 Å cutoff around graphene atoms, as obtained from the MD annealing simulations. The results demonstrate that hydrogen dissociative chemisorption on Pt induces an increase in the Pt–graphene separation distance. Although these changes are small (on the order of tens of mÅ under our MD simulation conditions), they exhibit a clear trend across different Pt loadings. From a sensing standpoint, this outcome corroborates that although graphene interacts only weakly with hydrogen, it can still detect hydrogen uptake through bonding changes at the Pt–graphene interface.

Table III provides the DFT (PBE) work functions for several hydrogenated Pt/graphene structures, along with their deviations from pristine graphene ($\phi_{\text{Gr}} = 4.62\,\text{eV}$) and the vertical separations between the Pt center-of-mass and graphene before and after hydrogenation. Al-

TABLE III. DFT (PBE) results for hydrogenated Pt structures on graphene. Columns list the Pt structure and the associated graphene supercell size, the work function on the graphene-facing side (ϕ) with its deviation from pristine graphene ($\phi_{\text{Gr}} = 4.62$ eV with PBE), and the vertical separation between Pt center-of-mass and graphene ($\Delta z_{Gr-Pt_{com}}$) before and after hydrogenation (values given as bare/H).

Pt structure (supercell size)	ϕ (eV)	$\Delta z_{Gr-Pt_{com}}$ (Å) (bare/H)
Pt Adatom		
2×2	4.55 (-0.07)	2.09/2.23
3×3	4.60 (-0.02)	2.16/2.25
4×4	4.59 (-0.03)	2.22/2.26
5×5	4.62 (0.00)	2.26/2.30
Pt Dimer		
2×2	4.47 (-0.15)	3.33/3.42
3×3	4.63 ($+0.01$)	3.40/3.49
4×4	4.64 ($+0.02$)	3.45/4.07
5×5	4.63 ($+0.01$)	3.47/4.05
Pt(111) Slab		
2×2	4.69 ($+0.07$)	7.24/7.30

though these DFT simulations assume one H adsorbate per surface Pt site, realistic conditions typically involve lower coverages, leading to less pronounced but still qualitatively consistent effects.

Upon H adsorption, the finite Pt structures exhibit a substantial increase in ϕ, often matching or exceeding the work function of pristine graphene. This increase is accompanied by an upward displacement of the Pt nanostructure, consistent with MLIP predictions (Figure S5). This behavior suggests that H withdraws electron density from the Pt clusters, thereby diminishing their electron-donating effect to graphene and effectively lifting them off the surface. The considerable rise in ϕ highlights hydrogen's capacity to suppress or even reverse the n-type doping of graphene induced by Pt nanoclusters. In contrast, the four-layer Pt(111) slab exhibits only a minor change in its work function, consistent with a bulk-like regime in which localized H adsorption has limited impact on the Pt-graphene interface due to stronger shielding by the thicker slab and inherently weaker Pt–graphene local binding.

Taken together, these findings confirm a sensing mechanism in which Pt nanoclusters n-dope graphene. Upon H adsorption on Pt surfaces, electrons are withdrawn from the clusters by H atoms, reducing their electron donation to graphene, thereby lowering its carrier concentration and increasing its resistance. Experimental studies on Pt-functionalized graphene H_2 sensors show that H_2 exposure leads to increased device resistance, matching this proposed mechanism[33].

Notably, as Pt loading increases, the net change in the Pt–graphene distance (final minus initial) decreases monotonically (Figure S5b). This implies that at lower coverages, smaller, undercoordinated Pt clusters—with stronger local Pt–graphene binding and thinner mor-

phologies—experience a more pronounced lift-off from the graphene surface upon hydrogen adsorption, thereby more effectively transducing H adsorption events from the H–Pt interface to the Pt–graphene interface. Although smaller clusters may exhibit weaker H–Pt interactions, they produce a more pronounced sensing signal than higher Pt coverages; however, under practical conditions with lower hydrogen concentrations, H–Pt interaction strength may become more critical. Moreover, while smaller Pt clusters more effectively transduce hydrogen adsorption into a measurable graphene response, they must also be sufficiently abundant to ensure adequate doping and stable signal output. Therefore, an intermediate Pt loading may offer the optimal balance to maximize sensitivity.

III. METHODS

DFT Calculations. DFT calculations were conducted using the Generalized Gradient Approximation (GGA) formulated by Perdew, Burke, and Ernzerhof (PBE) along with Projector Augmented Wave (PAW) pseudopotentials, using VASP[79–82]. Collinear spin-polarized calculations are performed, with a plane wave basis cutoff at 520 eV. Integration over the first Brillouin zone is accomplished using a uniform Monkhorst-Pack mesh with a density of approximately 8.1 Å^{-1}[83]. The self-consistent field (SCF) loop is terminated when the energy change falls below 10^{-5} eV. Dispersion interactions were addressed after the VASP calculations using the DFT-D3 method with a cutoff of 6.5 Å, consistent with the MLIP cutoff radius. A rational damping function, modified from the original by Becke and Johnson, was employed as implemented in the simple-dftd3 package[84]. The rational damping function ensures that the dispersion energy approaches a finite value rather than being eliminated at short distances[85].

Machine Learning Interatomic Potential Training. We employ the Allegro framework for our machine learning interatomic potential (MLIP)[36,37], with a cutoff radius $r_{max} = 6.5$ Å, maximum order used in spherical harmonics embedding $l_{max} = 2$, full O_3 parity symmetry, and one tensor product layer with 32 features. We utilized a two-body latent multilayer perceptron (MLP) and a later stage latent MLP with hidden dimensions $[32, 64, 128]$ and $[128, 128, 128]$ respectively, both featuring the SiLU (Sigmoid Linear Unit) activation function[86]. For the final edge energy MLP, a single hidden layer of dimension 32 without nonlinearity was used. The interatomic distances were embedded using a trainable per-ordered-species-pair radial basis of 6 Bessel functions and a polynomial cutoff envelope function as specified in[36]. The loss function employed involves the mean squared error of both atomic forces and per-atom energies, with equal weighting assigned to both components.

The learning rate was set to 4×10^{-4}, the training batch size was 5, and the default Adam optimizer in PyTorch was utilized[87,88]. A repulsive Ziegler-Biersack-Littmark (ZBL) term was added to Allegro to enhance the stability of the MLIP at very small interatomic distances[89].

Our dataset consists of a total of $5,053$ structures: $3,848$ Pt/graphene, 680 H/Pt/graphene, 464 Pt-only, and 61 H-only structures. This results in $121,318$ C, $54,066$ Pt, and $18,656$ H local atomic environments. All structures maintain DFT force components ≤ 40 eV/Å and have negative DFT cohesive energies.

Minima Hopping. The MH simulations were conducted using a version of the ASE MH tool that we specifically adapted for the Pt_N/graphene systems[90,91]. The MD search phase in MH focused exclusively on Pt_N clusters, while the graphene substrate was reintroduced during the energy minimization phase. Each MD search is initiated at a high temperature of 5000 K and concluded after identifying 4 PES minima. A newly identified minimum was considered acceptable if the energy difference from the previous minimum was less than 2.5 eV. Energy minimizations were conducted until the forces on all atoms were reduced to below 0.02 eV/Å.

Molecular Dynamics Simulations. All MD simulations were performed using LAMMPS with the Allegro pair style[36,92,93]. The Nosé-Hoover NVT ensemble was employed, with a time step of $dt = 2$ fs for Pt/graphene simulations and $dt = 1$ fs for reactive simulations involving hydrogen. Velocity rescaling was applied every $100 \times dt$, and initial velocities were sampled from a Boltzmann distribution corresponding to the target temperature.

In Pt growth simulations on graphene, newly deposited Pt atoms were introduced prior to the MD simulation. They were initially positioned at $z \geq 3.2$ Å above the highest local Pt/C atom (within a local in-plane cutoff radius of 5.0 Å to account for graphene local corrugations), with x and y coordinates randomly assigned within the supercell while maintaining a minimum separation of 2.8 Å from all pre-existing atoms. In H/Pt/graphene simulations, H_2 molecules with an H-H bond length of 0.75 Å were initially placed atop the optimized Pt/graphene structure at 5.0–20.0 Å above the highest Pt atom, while ensuring an initial intermolecular separation of at least 4.0 Å between H_2 molecules.

To emulate a rigid substrate, the net linear momentum of the graphene sheet was zeroed at each timestep. In subsequent hydrogen-reactive simulations, where H_2 molecules were introduced at initial high pressure, the net linear momentum of each Pt cluster was also zeroed at each timestep to mitigate artificial drift under intense hydrogen impingement while still allowing local atomic rearrangements and preserving realistic kinetics.

Experimental Pt Functionalization. Monolayer CVD graphene on SiO_2 substrate was commercially pur-

chased and used in the analysis (Alpha Graphene inc.). All samples were annealed at 200 °C for 1 hour under vacuum to remove any residual organics and eliminate adsorbed oxygen and water molecules. This process also ensures strong and uniform adhesion between the graphene and functionalized Pt and hinders unwanted interfacial reactions. The functionalization of the monolayer graphene was performed using electron-beam evaporation. Pt deposition was carried out at a rate of 0.05 Å/s using an Angstrom electron-beam evaporator under a vacuum of 7×10^{-7} torr. Two different Pt thicknesses (0.4 nm and 1.0 nm) were targeted and measured using a crystal monitor. This ultrathin Pt thickness was optimized to form uniform Pt clusters on the graphene surface without completely coating the graphene film with a continuous Pt layer. The goal was to create distinct catalytic functionalization sites on the graphene surface.

For calibration and characterization, a reference graphene sample on a TEM grid (2000 mesh copper grid, Ted Pella inc.) was placed inside the electron-beam chamber to monitor the quality of the Pt deposition and aid in optimizing the Pt functionalization.

TEM & Raman Characterization. The morphology and structural properties of the Pt-functionalized graphene were investigated using TEM. TEM imaging was performed using a JEOL JEM 2100 microscope with an accelerating voltage of 200 kV. HRTEM was employed to examine the structural properties of the deposited Pt nanostructures on the graphene surface. A SAED pattern was also obtained to assess the crystallinity of the Pt clusters and determine their crystallographic orientation on graphene.

Additionally, Raman spectroscopy (Horiba) was performed using a 532 nm laser to evaluate the quality of the graphene before and after Pt functionalization.

IV.   DATA & CODE AVAILABILITY

The DFT training dataset, MLIP configuration, and MD simulation and analysis workflows are publicly available in the GitHub repository at `https://github.com/akram-ibrahim/MLIP-GrPt_CrystGrow-H2React`.

V.   REFERENCES

[1] P. Recum and T. Hirsch, "Graphene-based chemiresistive gas sensors," Nanoscale Advances **6**, 11–31 (2024).

[2] C. Wang, Y. Wang, Z. Yang, and N. Hu, "Review of recent progress on graphene-based composite gas sensors," Ceramics International **47**, 16367–16384 (2021).

[3] S. S. Varghese, S. Lonkar, K. Singh, S. Swaminathan, and A. Abdala, "Recent advances in graphene based gas sensors," Sensors and Actuators B: Chemical **218**, 160–183 (2015).

[4] S. Basu and P. Bhattacharyya, "Recent developments on graphene and graphene oxide based solid state gas sensors," Sensors and Actuators B: Chemical **173**, 1–21 (2012).

[5] Z. Chen, J. Wang, and Y. Wang, "Strategies for the performance enhancement of graphene-based gas sensors: A review," Talanta **235**, 122745 (2021).

[6] K. I. Bolotin, K. Sikes, Z. Jiang, M. Klima, G. Fudenberg, J. Hone, P. Kim, and H. L. Stormer, "Ultrahigh electron mobility in suspended graphene," Solid state communications **146**, 351–355 (2008).

[7] A. H. Castro Neto, F. Guinea, N. M. Peres, K. S. Novoselov, and A. K. Geim, "The electronic properties of graphene," Reviews of modern physics **81**, 109–162 (2009).

[8] D. Acharyya and P. Bhattacharyya, "Functionalization of graphene and its derivatives for developing efficient solid-state gas sensors: Trends and challenges," Functional Nanomaterials: Advances in Gas Sensing Technologies , 245–284 (2020).

[9] A. A. Balandin, "Low-frequency 1/f noise in graphene devices," Nature nanotechnology **8**, 549–555 (2013).

[10] J. H. Gosling, O. Makarovsky, F. Wang, N. D. Cottam, M. T. Greenaway, A. Patanè, R. D. Wildman, C. J. Tuck, L. Turyanska, and T. M. Fromhold, "Universal mobility characteristics of graphene originating from charge scattering by ionised impurities," Communications Physics **4**, 30 (2021).

[11] G. Gao, D. Liu, S. Tang, C. Huang, M. He, Y. Guo, X. Sun, and B. Gao, "Heat-initiated chemical functionalization of graphene," Scientific reports **6**, 20034 (2016).

[12] X. Ye, M. Qi, H. Yang, F. S. Mediko, H. Qiang, Y. Yang, and C. He, "Selective sensing and mechanism of patterned graphene-based sensors: Experiments and dft calculations," Chemical Engineering Science **247**, 117017 (2022).

[13] Z. D. Leve, E. I. Iwuoha, and N. Ross, "The synergistic properties and gas sensing performance of functionalized graphene-based sensors," Materials **15**, 1326 (2022).

[14] B. Liu, Z. Han, A. Bendavid, P. J. Martin, P. V. Kumar, Y. Haghshenas, M. Alamri, and J. Z. Wu, "Atomic-layer deposition of the single-atom pt catalyst on vertical graphene for h2 sensing," ACS Applied Nano Materials **7**, 22605–22616 (2024).

[15] A. V. Singhal, H. Charaya, and I. Lahiri, "Noble metal decorated graphene-based gas sensors and their fabrication: a review," Critical Reviews in Solid State and Materials Sciences **42**, 499–526 (2017).

[16] S. G. Chatterjee, S. Chatterjee, A. K. Ray, and A. K. Chakraborty, "Graphene–metal oxide nanohybrids for toxic gas sensor: A review," Sensors and Actuators B: Chemical **221**, 1170–1181 (2015).

[17] F.-L. Meng, Z. Guo, and X.-J. Huang, "Graphene-based hybrids for chemiresistive gas sensors," TrAC Trends in Analytical Chemistry **68**, 37–47 (2015).

[18] M. K. Singla, P. Nijhawan, and A. S. Oberoi, "Hydrogen fuel and fuel cell technology for cleaner future: a review," Environmental Science and Pollution Research **28**, 15607–15626 (2021).

[19] J. Manna, P. Jha, R. Sarkhel, C. Banerjee, A. Tripathi, and M. Nouni, "Opportunities for green hydrogen production in petroleum refining and ammonia synthesis industries in india," international journal of hydrogen energy **46**, 38212–38231 (2021).

[20] T. Mikal-Evans, N. Madhusudhan, J. Dittmann, M. N. Günther, L. Welbanks, V. Van Eylen, I. J. Crossfield, T. Daylan, and L. Kreidberg, "Hubble space telescope transmission spectroscopy for the temperate sub-neptune toi-270 d: A possible hydrogen-rich atmosphere containing water vapor," The Astronomical Journal **165**, 84 (2023).

[21] W. J. Buttner, M. B. Post, R. Burgess, and C. Rivkin, "An overview of hydrogen safety sensors and requirements," International Journal of Hydrogen Energy **36**, 2462–2470 (2011).

[22] R. Wadhwa, A. Kumar, R. Sarkar, P. P. Mohanty, D. Kumar, S. Deswal, P. Kumar, R. Ahuja, S. Chakraborty, M. Kumar, *et al.*, "Pt nanoparticles on vertically aligned large-area mos2 flakes for selective h2 sensing at room temperature," ACS Applied Nano Materials **6**, 2527–2537 (2023).

[23] D. Del Orbe Henriquez, I. Cho, H. Yang, J. Choi, M. Kang, K. S. Chang, C. B. Jeong, S. W. Han, and I. Park, "Pt nanostructures fabricated by local hydrothermal synthesis for low-power

catalytic-combustion hydrogen sensors," ACS Applied Nano Materials **4**, 7–12 (2020).

[24] A. Kumar, Y. Zhao, M. M. Mohammadi, J. Liu, T. Thundat, and M. T. Swihart, "Palladium nanosheet-based dual gas sensors for sensitive room-temperature hydrogen and carbon monoxide detection," ACS sensors **7**, 225–234 (2022).

[25] A. Kumar, T. Thundat, and M. T. Swihart, "Ultrathin palladium nanowires for fast and hysteresis-free h2 sensing," ACS Applied Nano Materials **5**, 5895–5905 (2022).

[26] R. Olsen, G. Kroes, and E. Baerends, "Atomic and molecular hydrogen interacting with pt (111)," The Journal of Chemical Physics **111**, 11155–11163 (1999).

[27] K. Christmann, G. Ertl, and T. Pignet, "Adsorption of hydrogen on a pt (111) surface," Surface Science **54**, 365–392 (1976).

[28] A. Sihag, Z.-L. Xie, H. V. Thang, C.-L. Kuo, F.-G. Tseng, M. S. Dyer, and H.-Y. T. Chen, "Dft insights into comparative hydrogen adsorption and hydrogen spillover mechanisms of pt4/graphene and pt4/anatase (101) surfaces," The Journal of Physical Chemistry C **123**, 25618–25627 (2019).

[29] A. Sihag, Y. Reyes, Y.-C. Lin, M. Dyer, and H.-Y. T. Chen, "How do defects affect hydrogen spillover on graphene-supported pt? a dft study," Materials Today Sustainability **24**, 100554 (2023).

[30] G. M. Psofogiannakis and G. E. Froudakis, "Dft study of the hydrogen spillover mechanism on pt-doped graphite," The Journal of Physical Chemistry C **113**, 14908–14915 (2009).

[31] F. Ruffino and F. Giannazzo, "A review on metal nanoparticles nucleation and growth on/in graphene," Crystals **7**, 219 (2017).

[32] L. Ferbel, S. Veronesi, Y. Vlamidis, A. Rossi, L. Sabattini, C. Coletti, and S. Heun, "Platinum-decorated graphene: Experimental insight into growth mechanisms and hydrogen adsorption properties," FlatChem **45**, 100661 (2024).

[33] Y. Kim, T. Kim, J. Lee, Y. S. Choi, J. Moon, S. Y. Park, T. H. Lee, H. K. Park, S. A. Lee, M. S. Kwon, et al., "Tailored graphene micropatterns by wafer-scale direct transfer for flexible chemical sensor platform," Advanced Materials **33**, 2004827 (2021).

[34] A. W. Robertson, G.-D. Lee, S. Lee, P. Buntin, M. Drexler, A. A. Abdelhafiz, E. Yoon, J. H. Warner, and F. M. Alamgir, "Atomic structure and dynamics of epitaxial platinum bilayers on graphene," ACS nano **13**, 12162–12170 (2019).

[35] A. Abdelhafiz, A. Vitale, C. Joiner, E. Vogel, and F. M. Alamgir, "Layer-by-layer evolution of structure, strain, and activity for the oxygen evolution reaction in graphene-templated pt monolayers," ACS applied materials & interfaces **7**, 6180–6188 (2015).

[36] A. Musaelian, S. Batzner, A. Johansson, L. Sun, C. J. Owen, M. Kornbluth, and B. Kozinsky, "Learning local equivariant representations for large-scale atomistic dynamics," Nature Communications **14**, 579 (2023).

[37] S. Batzner, A. Musaelian, L. Sun, M. Geiger, J. P. Mailoa, M. Kornbluth, N. Molinari, T. E. Smidt, and B. Kozinsky, "E (3)-equivariant graph neural networks for data-efficient and accurate interatomic potentials," Nature communications **13**, 2453 (2022).

[38] M. Geiger and T. Smidt, "e3nn: Euclidean neural networks," arXiv preprint arXiv:2207.09453 (2022).

[39] J. Behler and G. Csányi, "Machine learning potentials for extended systems: a perspective," The European Physical Journal B **94**, 1–11 (2021).

[40] P. Friederich, F. Häse, J. Proppe, and A. Aspuru-Guzik, "Machine-learned potentials for next-generation matter simulations," Nature Materials **20**, 750–761 (2021).

[41] A. Ibrahim, D. Wines, and C. Ataca, "Modeling chemical exfoliation of non-van der waals chromium sulfides by machine learning interatomic potentials and monte carlo simulations," The Journal of Physical Chemistry C **128**, 1267–1283 (2024).

[42] X. Chen, N. Q. Le, and P. Clancy, "Diffusion-limited crystal growth of gallium nitride using active machine learning," Crystal Growth & Design **24**, 2855–2863 (2024).

[43] J. Vandermause, Y. Xie, J. S. Lim, C. J. Owen, and B. Kozinsky, "Active learning of reactive bayesian force fields applied to heterogeneous catalysis dynamics of h/pt," Nature Communications **13**, 5183 (2022).

[44] C. J. Owen, L. Russotto, C. R. O'Connor, N. Marcella, A. Johansson, A. Musaelian, and B. Kozinsky, "Atomistic evolution of active sites in multi-component heterogeneous catalysts," arXiv preprint arXiv:2407.13607 (2024).

[45] Y. Shaidu, W. DeSnoo, A. Smith, E. Taw, and J. B. Neaton, "Entropic effects on diamine dynamics and co2 capture in diamine-appended mg2 (dopbdc) metal–organic frameworks," The Journal of Physical Chemistry Letters **15**, 1130–1134 (2024).

[46] M. Krummenacher, M. Gubler, J. A. Finkler, H. Huber, M. Sommer-Jörgensen, and S. Goedecker, "Performing highly efficient minima hopping structure predictions using the atomic simulation environment (ase)," SoftwareX **25**, 101632 (2024).

[47] G. Henkelman, B. P. Uberuaga, and H. Jónsson, "A climbing image nudged elastic band method for finding saddle points and minimum energy paths," The Journal of chemical physics **113**, 9901–9904 (2000).

[48] A. Luntz, J. Brown, and M. Williams, "Molecular beam studies of h2 and d2 dissociative chemisorption on pt (111)," The Journal of chemical physics **93**, 5240–5246 (1990).

[49] N. B. Arboleda Jr, H. Kasai, W. A. Dino, and H. Nakanishi, "Potential energy of h2 dissociation and adsorption on pt (111) surface: First-principles calculation," Japanese Journal of Applied Physics **46**, 4233 (2007).

[50] G. Herzberg and A. Monfils, "The dissociation energies of the h2, hd, and d2 molecules," Journal of Molecular Spectroscopy **5**, 482–498 (1961).

[51] Y. Miura, H. Kasai, W. Dino, H. Nakanishi, and T. Sugimoto, "First principles studies for the dissociative adsorption of h 2 on graphene," Journal of applied physics **93**, 3395–3400 (2003).

[52] M. Aliofkhazraei and N. Ali, "7.05 - fabrication of micro/nanostructured coatings by cvd techniques," in *Comprehensive Materials Processing* (Elsevier, Oxford, 2014) pp. 85–117.

[53] A. Stukowski, "Visualization and analysis of atomistic simulation data with ovito–the open visualization tool," Modelling and simulation in materials science and engineering **18**, 015012 (2009).

[54] X. Liu, C.-Z. Wang, M. Hupalo, W. Lu, M. C. Tringides, Y. Yao, and K.-M. Ho, "Metals on graphene: correlation between adatom adsorption behavior and growth morphology," Physical chemistry chemical physics **14**, 9157–9166 (2012).

[55] X. Liu, Y. Han, J. W. Evans, A. K. Engstfeld, R. J. Behm, M. C. Tringides, M. Hupalo, H.-Q. Lin, L. Huang, K.-M. Ho, et al., "Growth morphology and properties of metals on graphene," Progress in Surface Science **90**, 397–443 (2015).

[56] S. Yamakawa, K. Okazaki-Maeda, M. Kohyama, and S. Hyodo, "Phase-field model for deposition process of platinum nanoparticles on carbon substrate," in *Journal of Physics: Conference Series*, Vol. 100 (IOP Publishing, 2008) p. 072042.

[57] M. Krone, J. E. Stone, T. Ertl, and K. Schulten, "Fast visualization of gaussian density surfaces for molecular dynamics and particle system trajectories." EuroVis (Short Papers) **10**, 067–071 (2012).

[58] M. Ester, H.-P. Kriegel, J. Sander, X. Xu, et al., "A density-based algorithm for discovering clusters in large spatial databases with noise." in *kdd*, Vol. 96 (1996) pp. 226–231.

[59] H. Edelsbrunner, D. Kirkpatrick, and R. Seidel, "On the shape of a set of points in the plane," IEEE Transactions on Information Theory **29**, 551–559 (1983).

[60] C. Meng, J. Gao, R. Li, Y. Ning, Y. Chang, R. Mu, Q. Fu, and X. Bao, "Step-confined thin film growth via near-surface atom migration," Nano Research **13**, 1552–1557 (2020).

[61] Y. Wei and Z. Sun, "Liquid-phase exfoliation of graphite for mass production of pristine few-layer graphene," Current opinion in colloid & interface science **20**, 311–321 (2015).

[62] P. M. Larsen, S. Schmidt, and J. Schiøtz, "Robust structural identification via polyhedral template matching," Modelling and Simulation in Materials Science and Engineering **24**, 055007 (2016).

[63] J. I. Choi, A. Abdelhafiz, P. Buntin, A. Vitale, A. W. Robertson, J. Warner, S. S. Jang, and F. M. Alamgir, "Contiguous and atomically thin pt film with supra-bulk behavior through

graphene-imposed epitaxy," Advanced Functional Materials **29**, 1902274 (2019).

[64] A. A. Saberi, "Recent advances in percolation theory and its applications," Physics Reports **578**, 1–32 (2015).

[65] R. Voggu, B. Das, C. S. Rout, and C. Rao, "Effects of charge transfer interaction of graphene with electron donor and acceptor molecules examined using raman spectroscopy and cognate techniques," Journal of Physics: Condensed Matter **20**, 472204 (2008).

[66] L. G. Cançado, V. P. Monken, J. L. E. Campos, J. C. Santos, C. Backes, H. Chacham, B. R. Neves, and A. Jorio, "Science and metrology of defects in graphene using raman spectroscopy," Carbon **220**, 118801 (2024).

[67] A. Abdelhafiz, A. Vitale, P. Buntin, B. deGlee, C. Joiner, A. Robertson, E. M. Vogel, J. Warner, and F. M. Alamgir, "Epitaxial and atomically thin graphene–metal hybrid catalyst films: the dual role of graphene as the support and the chemically-transparent protective cap," Energy & Environmental Science **11**, 1610–1616 (2018).

[68] J. T. Gudmundsson, A. Anders, and A. Von Keudell, "Foundations of physical vapor deposition with plasma assistance," Plasma Sources Science and Technology **31**, 083001 (2022).

[69] A. Picone, M. Riva, G. Fratesi, A. Brambilla, G. Bussetti, M. Finazzi, L. Duo, and F. Ciccacci, "Enhanced atom mobility on the surface of a metastable film," Physical Review Letters **113**, 046102 (2014).

[70] A. Dumi, S. Upadhyay, L. Bernasconi, H. Shin, A. Benali, and K. D. Jordan, "The binding of atomic hydrogen on graphene from density functional theory and diffusion monte carlo calculations," The Journal of Chemical Physics **156** (2022).

[71] C.-H. Yeh, H. V. Thang, Y. I. A. Reyes, C. Coluccini, and H.-Y. T. Chen, "Dft insights into hydrogen spillover mechanisms: Effects of metal species, size, and support," The Journal of Physical Chemistry C (2025).

[72] D. Chodvadiya, S. Kanabar, B. Chakraborty, and P. K. Jha, "Exploring the hydrogen storage possibility of the pristine, defected and metals decorated o-b2n2 monolayers: insights from dft simulations," International Journal of Hydrogen Energy **53**, 958–968 (2024).

[73] P. Khomyakov, G. Giovannetti, P. Rusu, G. v. Brocks, J. Van den Brink, and P. J. Kelly, "First-principles study of the interaction and charge transfer between graphene and metals," Physical Review B—Condensed Matter and Materials Physics **79**, 195425 (2009).

[74] J.-T. Seo, J. Bong, J. Cha, T. Lim, J. Son, S. H. Park, J. Hwang, S. Hong, and S. Ju, "Manipulation of graphene work function using a self-assembled monolayer," Journal of Applied Physics **116** (2014).

[75] J. Zheng, Y. Wang, L. Wang, R. Quhe, Z. Ni, W.-N. Mei, Z. Gao, D. Yu, J. Shi, and J. Lu, "Interfacial properties of bilayer and trilayer graphene on metal substrates," Scientific reports **3**, 2081 (2013).

[76] M. Legesse, F. El Mellouhi, E. T. Bentria, M. E. Madjet, T. S. Fisher, S. Kais, and F. H. Alharbi, "Reduced work function of graphene by metal adatoms," Applied Surface Science **394**, 98–107 (2017).

[77] K. T. Chan, J. Neaton, and M. L. Cohen, "First-principles study of metal adatom adsorption on graphene," Physical Review B—Condensed Matter and Materials Physics **77**, 235430 (2008).

[78] G. Ramos-Sanchez and P. Balbuena, "Interactions of platinum clusters with a graphite substrate," Physical Chemistry Chemical Physics **15**, 11950–11959 (2013).

[79] P. Hohenberg and W. Kohn, "Inhomogeneous electron gas," Physical review **136**, B864 (1964).

[80] J. P. Perdew, K. Burke, and M. Ernzerhof, "Generalized gradient approximation made simple," Physical review letters **77**, 3865 (1996).

[81] P. E. Blöchl, "Projector augmented-wave method," Physical review B **50**, 17953 (1994).

[82] G. Kresse and J. Furthmüller, "Efficient iterative schemes for ab initio total-energy calculations using a plane-wave basis set," Physical review B **54**, 11169 (1996).

[83] H. J. Monkhorst and J. D. Pack, "Special points for brillouin-zone integrations," Physical review B **13**, 5188 (1976).

[84] S. Ehlert, "Simple dft-d3: Library first implementation of the d3 dispersion correction," Journal of Open Source Software **9**, 7169 (2024).

[85] S. Grimme, S. Ehrlich, and L. Goerigk, "Effect of the damping function in dispersion corrected density functional theory," Journal of computational chemistry **32**, 1456–1465 (2011).

[86] S. Elfwing, E. Uchibe, and K. Doya, "Sigmoid-weighted linear units for neural network function approximation in reinforcement learning," Neural networks **107**, 3–11 (2018).

[87] D. P. Kingma and J. Ba, "Adam: A method for stochastic optimization," arXiv preprint arXiv:1412.6980 (2014).

[88] A. Paszke, S. Gross, F. Massa, A. Lerer, J. Bradbury, G. Chanan, T. Killeen, Z. Lin, N. Gimelshein, L. Antiga, *et al.*, "Pytorch: An imperative style, high-performance deep learning library," Advances in neural information processing systems **32** (2019).

[89] J. F. Ziegler and J. P. Biersack, "The stopping and range of ions in matter," in *Treatise on heavy-ion science: volume 6: astrophysics, chemistry, and condensed matter* (Springer, 1985) pp. 93–129.

[90] A. A. Peterson, "Global optimization of adsorbate–surface structures while preserving molecular identity," Topics in Catalysis **57**, 40–53 (2014).

[91] A. H. Larsen, J. J. Mortensen, J. Blomqvist, I. E. Castelli, R. Christensen, M. Dułak, J. Friis, M. N. Groves, B. Hammer, C. Hargus, *et al.*, "The atomic simulation environment—a python library for working with atoms," Journal of Physics: Condensed Matter **29**, 273002 (2017).

[92] A. P. Thompson, H. M. Aktulga, R. Berger, D. S. Bolintineanu, W. M. Brown, P. S. Crozier, P. J. in 't Veld, A. Kohlmeyer, S. G. Moore, T. D. Nguyen, R. Shan, M. J. Stevens, J. Tranchida, C. Trott, and S. J. Plimpton, "LAMMPS - a flexible simulation tool for particle-based materials modeling at the atomic, meso, and continuum scales," Comp. Phys. Comm. **271**, 108171 (2022).

[93] S. Plimpton, "Fast parallel algorithms for short-range molecular dynamics," Journal of computational physics **117**, 1–19 (1995).

VI. COMPETING INTERESTS

The authors declare no competing interests.

VII. ADDITIONAL INFORMATION

Supplementary information is available for this paper.

Supporting Information

Data-Driven Molecular Dynamics and TEM Analysis of Platinum Crystal Growth on Graphene and Reactive Hydrogen-Sensing Dynamics

Akram Ibrahim,[†] Ahmed M. Hafez,[‡] Mahmooda Sultana,[§] and Can Ataca[*,†]

[†]Department of Physics, University of Maryland Baltimore County, Baltimore, Maryland 21250, United States

[‡]Center for Research and Exploration in Space Science and Technology, NASA Goddard Space Flight Center, Greenbelt, Maryland 20771, United States

[¶]Department of Astronomy, University of Maryland College Park, College Park, Maryland 20742, United States

[§]Planetary Environments Laboratory, NASA Goddard Space Flight Center, Greenbelt, Maryland 20771, United States
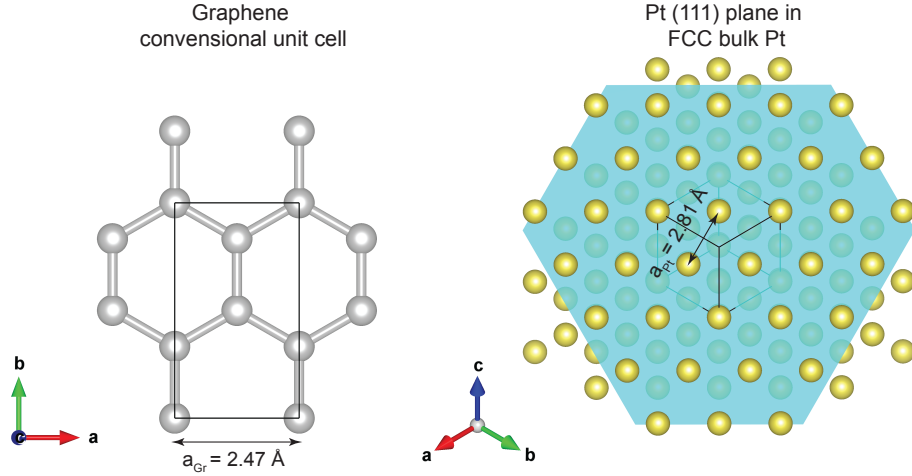
E-mail: ataca@umbc.edu

Figure S1: **Schematic representations of the DFT-relaxed conventional (rectangular) graphene unit cell and the Pt (111) plane in FCC bulk Pt.**

Graphene and Pt have lattice mismatch ($a_{\mathrm{Gr}} = 2.468\,\text{Å}$ and $a_{\mathrm{Pt}} = 2.805\,\text{Å}$), where a_{Gr} represents graphene's lattice constant and a_{Pt} represents the nearest neighbor Pt–Pt distance measured in bulk FCC Pt. Assuming a nearly-square graphene supercell of size N along the zigzag direction, the supercell dimensions along the x and y directions (with zigzag along the x-axis and armchair along the y-axis) are given by $N_x = N$ and $N_y = \frac{N}{\sqrt{3}}$. The area of the graphene conventional unit cell is $A_{\mathrm{Gr\ unit}} = a_{\mathrm{Gr}}^2 \sqrt{3}$. Likewise, for a unit cell of a close-packed arrangement of Pt atoms, the area is $A_{\mathrm{Pt\ unit}} = a_{\mathrm{Pt}}^2 \sqrt{3}$. Thus, the graphene supercell area is $A_{\mathrm{Gr\ super}} = N_x \times N_y \times a_{\mathrm{Gr}}^2 \sqrt{3}$. For a close-packed Pt monolayer covering the graphene area, the number of Pt unit cells is $A_{\mathrm{Gr\ super}}/A_{\mathrm{Pt\ unit}}$, and since each conventional unit cell of the close-packed Pt monolayer contains 2 Pt atoms, the total number of Pt atoms is $N_{\mathrm{Pt}} = A_{\mathrm{Gr\ super}}/A_{\mathrm{Pt\ unit}} \times 2$. Thus, the number of atoms to make a close-packed Pt monolayer that covers the graphene area is $N_{\mathrm{Pt}} = N_x \times N_y \times \left(\frac{a_{\mathrm{Gr}}}{a_{\mathrm{Pt}}}\right)^2 \times 2$. For example, if $N_x = 60$ and $N_y = 35$, then $N_{\mathrm{Pt}} = 60 \times 35 \times \left(\frac{2.468\,\text{Å}}{2.805\,\text{Å}}\right)^2 \times 2 \approx 3249$.

Table S1: Pt/Graphene Cluster Statistics at Various Pt Loadings.

Pt Loading (ML)	Pt Count	#Clusters	Size Range	Thickness Range (nm)	Projected Area Fraction
0.25	812	12	16–166	0.6–1.3	0.045
0.50	1624	13	13–319	0.6–1.6	0.088
0.75	2436	12	4–475	0.3–1.5	0.127
1.00	3248	11	36–551	0.7–1.5	0.176
1.25	4060	11	33–721	0.6–1.8	0.219
1.50	4872	11	2–1630	0.0–1.8	0.254
1.75	5684	9	1–1833	0.0–1.8	0.296
2.00	6496	8	12–1939	0.3–1.9	0.323
2.25	7308	7	58–2107	0.9–1.9	0.365
2.50	8120	4	8–8014	0.3–2.3	0.386

Figure S2: **Cluster Properties versus Pt Loading. a** Projected area fraction (Pt clusters' projected area divided by graphene area). **b** Minimum and maximum cluster thickness versus Pt loading. **c** Number of clusters formed at different Pt loadings on graphene. **d** Minimum and maximum cluster size versus Pt loading. The same data are reported in Table S1.

Table S2: DFT+D3 cohesive energies and lattice parameters of various Pt bilayer structural models.

Model	Cohesive Energy (eV/atom)	a (Å)	b (Å)	d (Å)
sq-sq-top	-4.858	2.60	2.60	2.53
sq-sq-center	-4.954	2.64	2.64	2.08
hex-hex-bridge	-5.186	2.68	2.33	2.44
hex-hex-top	-5.188	2.68	2.32	2.63
hex-hex-center	-5.193	2.69	2.33	2.41
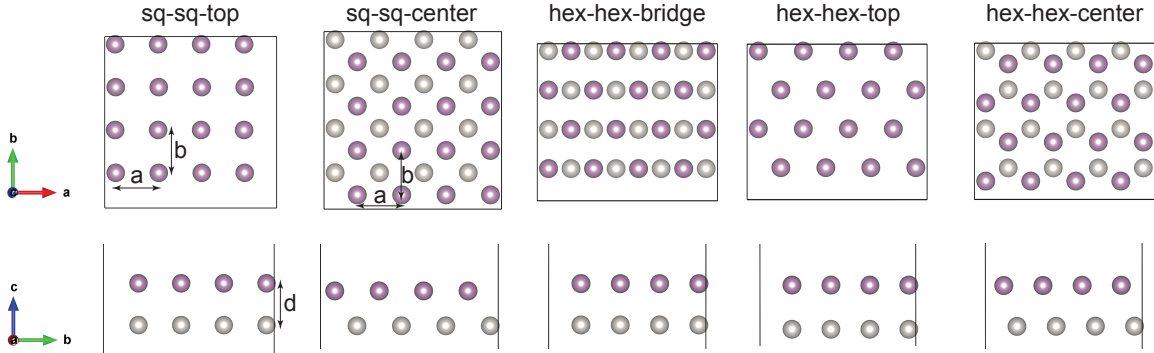
Figure S3: **Schematic representations of DFT-relaxed, free-standing Pt bilayer models.** The figure displays Pt bilayer models with both square (sq) and hexagonal (hex) in-plane arrangements. Distinct stable second-layer stacking configurations (top, center, and bridge) are highlighted in violet atop the silver-colored first layer. Cohesive energies and lattice constants are detailed in Table S2.
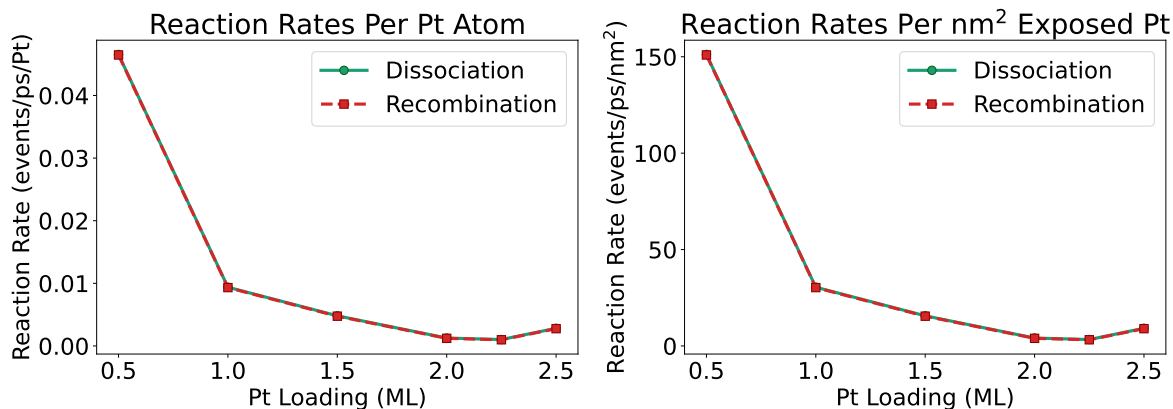
Figure S4: **Reaction Kinetics on Pt/Graphene Structures.** Reaction rates for hydrogen dissociation ($H_2 \rightarrow 2H$) and recombination ($2H \rightarrow H_2$) as functions of Pt loading. Rates are normalized per Pt atom in **a** and by the exposed Pt surface area (nm^2) in **b**.

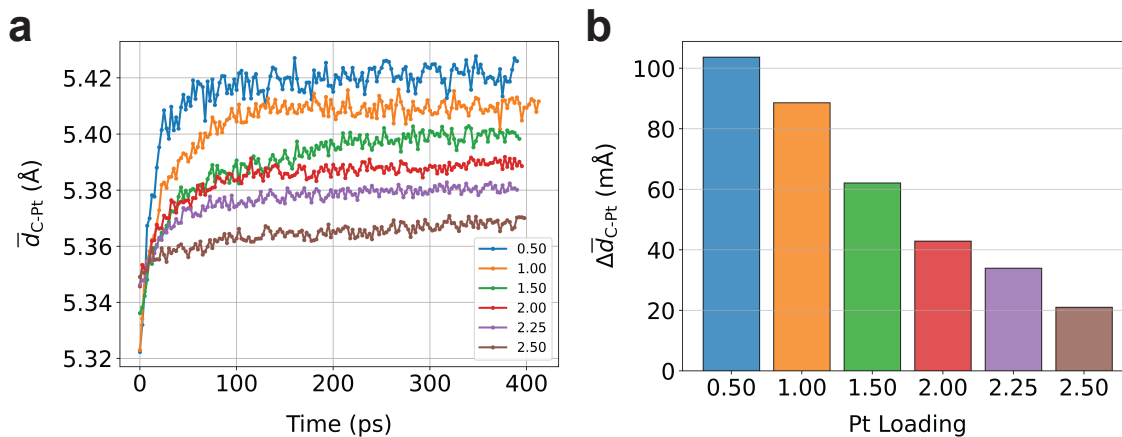
Figure S5: **Evolution of the Average Pt–C Distance Under Hydrogen Exposure.** (a) Time evolution of the average Pt–C distance (within a 6.5 Å cutoff) for various Pt loadings. (b) Net change in Pt–C distance (in milli-Å) between the initial and final MD configurations.

Table S3: SAED d-spacings and their corresponding reflection planes.

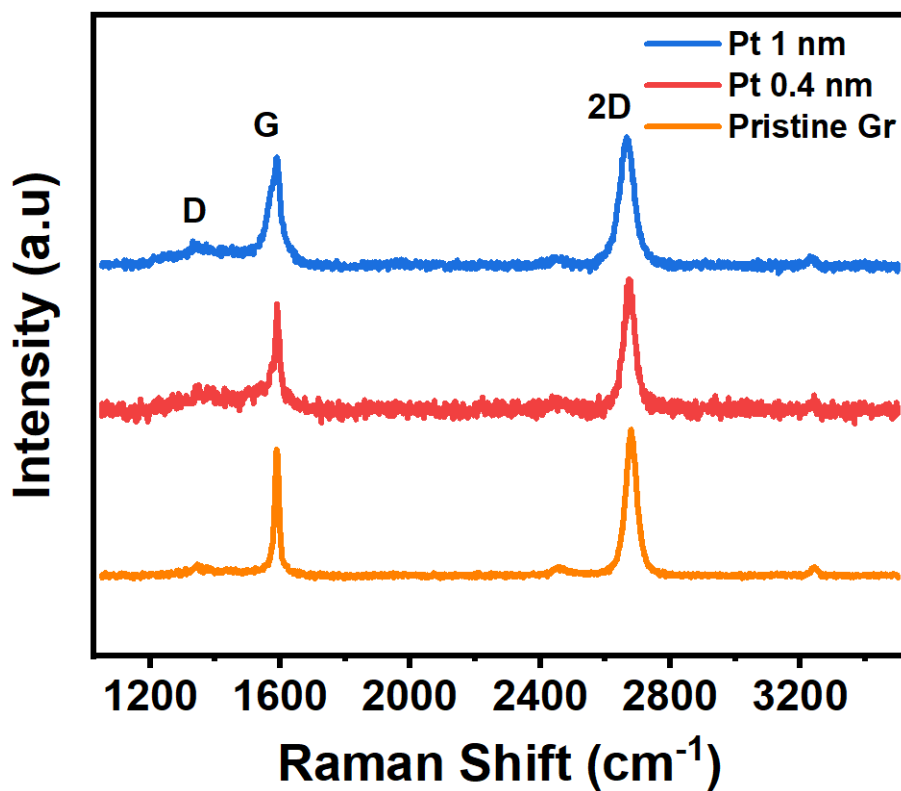| Ring No.	d-spacing (nm)	(hkl)
1	0.31	FCC (110)
2	0.25	SC (100)
3	0.21	Gr (100)
4	0.15	SC (110)
5	0.13	FCC (220)
6	0.12	Gr (110)
7	0.108	Gr (200)

Figure S6: Raman shift for pristine graphene (orange), Pt 0.4 nm (red), and Pt 1 nm (blue).